AOA Localization for Vehicle-Tracking Systems Using a Dual-Band Sensor Array

Mohammed Abdullah Ghali Al-Sadoon[ORCID], *Member, IEEE*, Rameez Asif,
Yasir Ismael Abdulraheem Al-Yasir[ORCID], *Member, IEEE*,
Raed A. Abd-Alhameed[ORCID], *Senior Member, IEEE*,
and Peter S. Excell, *Life Senior Member, IEEE*

Abstract—The issue of asset tracking in dense environments where the performance of the global positioning system (GPS) becomes unavailable or unreliable is addressed. The proposed solution uses a low-profile array of antenna elements (sensors) mounted on a finite conducting ground. A compact-size sensor array of six electrically small dual-band omnidirectional spiral antenna elements was designed as a front end of a tracker to operate in the 402 and 837 MHz spectrum bands. For the lower band, a three-element superposition method is applied to support estimation of the angle of arrival (AOA), whereas all six sensors are employed for the higher band. A low complexity and accurate AOA determination algorithm is proposed, the projection vector (PV), and this is combined with the array mentioned. Orthogonal frequency division multiplexing (OFDM) is integrated with the PV technique to increase the estimation resolution. The system was found to be suitable for installation on the roof of vehicles to localize the position of assets. The proposed system was tested for the tracking of nonstationary sources, and then two scenarios were investigated using propagation modeling software: outdoor to outdoor and outdoor to indoor. The results confirm that the proposed tracking system works efficiently with a single snapshot.

Index Terms—Angle of arrival (AOA) estimation, dual-band sensor array, multipath propagation, orthogonal frequency division multiplexing (OFDM), vehicle tracking, wideband localization system.

I. Introduction

POSITION awareness is an active research topic, and plays an essential role in various fields, for instance, localization applications, search-and-rescue operations, and tracking systems [1]–[4]. In addition, the Federal Communications

Mohammed Abdullah Ghali Al-Sadoon and Raed A. Abd-Alhameed are with the Faculty of Engineering and Informatics, University of Bradford, Bradford BD7 1DP, U.K., and also with the Department of Communication and Informatics Engineering, Basrah University College of Science and Technology, Basra 61004, Iraq (e-mail: m.a.g.al-sadoon@bradford.ac.uk).

Rameez Asif and Yasir Ismael Abdulraheem Al-Yasir are with the Faculty of Engineering and Informatics, University of Bradford, Bradford BD7 1DP, U.K.

Peter S. Excell is with the Faculty of Arts Science and Technology, Wrexham Glyndwr University, Wrexham LL11 2AW, U.K.

Commission (FCC) requires wireless network operators to determine the location of mobile subscribers within a few meters for emergency 911 call tracing [5]. In a tracking system, it is very desirable that both the transmitter and receiver sensor arrays are small and discrete. In practice, tracking systems might employ more than one localization solution such as a combination of radio frequency (RF) [6] and the global positioning system (GPS) [7], the antenna for the latter competing for available space with the sensor array. Although GPS is an effective technology that can give precise position-awareness around the world, its effectiveness drops in harsh environments, for example, in caves, in "urban canyons" under tree canopies and inside buildings [8]. This is because most GPS signals cannot penetrate such obstructions [9]. Thus, new approaches to position determination are required for use in such environments. A wideband localization system is an alternative solution to provide an accurate location in GPS-denied environments [10], [11].

In general, position-aware networks are made up of two categories, namely, anchors and agents. The location of the former can be obtained from the GPS or operator network, while the locations of the latter are mostly unidentified and their locations need to be found. To find their locations and directions under multipath propagation conditions, every node requires a wideband transceiver; thus, a positioning system could be accomplished using radio signaling between agents and their neighboring anchors. Localizing a target requires many signals to be sent from its transponder antennas and the associated position of the tracked object can then be identified from these signals using the variability of waveform matrices. As a result of potential physical obstacles in the line-of-sight (LOS) path, a non-LOS (NLOS) circumstance can result: in this situation, multipath and fading issues arise, and the attenuated signal is also more likely to suffer interference. However, location parameters can still be obtained, based on the nature of wave propagation, utilizing received signal strength (RSS), time of arrival/difference of arrival (TOA/TDOA), and angle of arrival (AOA) approaches [12]–[15]. Due to the properties of the propagation medium, the TOA approach requires a knowledge of the nature and dielectric properties of various penetrable building materials to estimate the Euclidean distance properly [16]. It has been analytically proven in [17] that neither TOA/TDOA nor RSS ranging techniques can achieve a positioning resolution with the required accuracy needed for safety applications. More notably, TOA/TDOA methods suffer from inaccurate synchronization, whereas RSS is very sensitive to shadowing and multipath effects since signal strength is attenuated with distance and by urban structures [18], [19].

AOA is an approach that estimates the arrival angles of the agents' signals arriving at the anchors (base stations) to determine their locations [20], [21]. To estimate AOA, only two elements are needed in a 2-D estimation, whereas three or more elements are required in a 3-D estimation. Due to the impinging signals being affected by random phenomena, for example, shadowing, scattering, and fading, the localization of a user's position can be uncertain. However, a wideband AOA system can determine not only the direction of the direct path from the emitter but also the angles of multiple paths, thus providing further information to use in determining the angles and the locations of targets. In the current state of the art, relatively few studies have investigated localization and tracking system accuracy under NLOS and multipath propagation conditions [22]–[24]. In [24], the information of the first arrival path was only exploited to estimate the arrival angle and neglected the other path coefficients. However, the direction of the first arrival path cannot always give the correct estimation direction of the tracked object. Other work in the literature uses a narrowband model, which basically utilizes averaging of the received paths and hence is not appropriate to wide bandwidth AOA systems [25]. In particular, the wideband AOA system provides precise and reliable direction estimation due to its robustness and fine delay precision in shadowing and harsh environments [26].

The traditional approaches to sensor antenna element design for very/ultra high-frequency (VHF/UHF) systems result in large physical structures, which are not suitable for tracking applications: they are also difficult to deploy. However, recently, the design of electrically small antennas for these frequencies has found increasing interest from researchers [27], [28]: these could be applied to reduce the sensor array size, which is crucial in many applications, typically needing to be as small as possible. One possible approach is to decrease the separation space between the elements of the sensor array. However, mutual coupling (MC) effects will increase and a decoupling approach would be required [29]. For tracking applications or in situations where random deployments are required, antennas with omnidirectional radiation patterns are more suitable [30], and this correlates with the use of electrically small elements. However, such elements (with small size relative to the wavelength) typically have high Q values and thus very narrow bandwidth. Therefore, applications such as the one presented in this article require improved designs of electrically small sensors for low-frequency use.

This article presents an efficient low-complexity localization system for tracking objects. A geometrically small omnidirectional dual-band array of spiral sensors for low-frequency applications is proposed: an array of six spiral sensors was designed and fabricated to work on both frequency bands. The distance between elements is made as small as possible and decoupling is applied. The advantage of proposing a dual-band array sensor in this work is to provide a strong judgment on the AOA over two spectrum bandwidths having different propagation characteristics. Thus, the AOA algorithm can obtain the directions of received signals based on two different frequencies simultaneously, or it can switch between them depending on which link provides a stronger connection in the tracking area.

The proposed sensor array is combined with a new-efficient direction-finding algorithm to determine the angles of the arriving paths. The orthogonal frequency division multiplexing (OFDM) scheme is integrated with the AOA method and used to combat multipath phenomena, with the received signals split into many small narrowband subcarriers to improve the estimation accuracy. The proposed system is planned to be deployed on the roof of cars for tracking and localization purposes. The system is first implemented to track a nonstationary object by utilizing a single snapshot to estimate its direction. The performance of the projection vector (PV) technique is compared with several AOA techniques and, subsequently, two scenarios are implemented: outdoor-to-outdoor and outdoor-to-indoor localization applications, each with multipath propagation. These scenarios are modeled using the Wireless-InSite software [31], in which multipath propagation and NLOS are considered and used to localize and track an agents' positions. The final decision on a target location considers the strongest signal strength, least TOA, and the average of all or some arriving subcarriers.

Throughout the rest of the paper, we have used boldface uppercase and lowercase symbols indicate matrixes and vectors, respectively, while lowercase symbols refer to scalar quantities. For superscripts, $(\cdot)^T$ refers to transpose, $(\cdot)^H$ represents transpose conjugate, $(\cdot)^{-1}$ denote inverse, while E{.} is the expected value. $(\bar{\cdot})$ and $(\check{\cdot})$ denote the real and imaginary parts of such a parameter. The remainder of this article is structured as follows. The AOA model with the proposed sensor array configuration is given in Section II. Section III provides the design and implementation of a dual-band spiral sensor element. The OFDM scheme model is presented in Section IV. Section V summarizes the principal working and modeling of the PV method and analyzes its complexity. The computer simulations, experimental results, and discussions are presented in Section VI. Section VII reviews the findings and gives the conclusion.

II. PROPOSED SENSOR ARRAY GEOMETRY FOR AOA

For omnidirectional coverage, the appropriate choice is a uniform ring array [32]. In several applications, the dimension of the antenna array should be as small as possible to suit the requirements of practicality and convenience. Typically, for tracking systems and localization purposes, it is most desirable to combine a small compact omnidirectional sensor array with an efficient AOA technique. Thus, a dual-band miniaturized sensor array having multiple spiral arms was proposed, having a maximum electrical size of $\lambda/3$ at the lower frequency band, as shown in Fig. 1: this array configuration is capable of working in dual-band mode. The separation distance between the three sensors (i.e., either 1, 3, 5 or 2, 4, 6) operated in the lower band (402 MHz) was set to be $d_1 = \lambda_{\text{lower}}/3 = 24.88$ cm. It should be noted that all six-sensor elements are used with the higher frequency band (837 MHz) in the signal processing stage, whereas only three elements (two different triangles) are used for the lower frequency band (402 MHz). The first triangle comprises sensors 1, 3, and 5, and the second one sensors 2, 4, and 6. The radius of the ring array (r) is $r = (0.5d_1/cos30°) = 14.36$ cm. For the higher band, $d_2 = 2rsin30°$, is also 14.36 cm.

From an array dimension point of view, the proposed dual-band sensor array occupies less space than if its elements were arranged in a circle for every single band. Thus, the higher band can use double the number of elements in the lower band with the same array size to provide better estimation accuracy and to track several targets simultaneously. Conversely, the lower band can be used for longer distances or environments that suffer from high penetration losses and thick
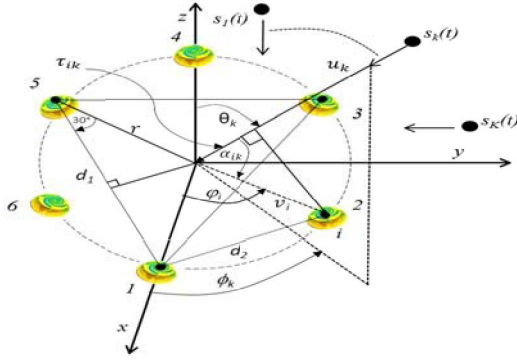
Fig. 1.   AOA modeling based on the proposed antenna array geometry.

obstacles. The array in Fig. 1 receives K signals from different directions and thus the measured data, $x(t)$, which includes the incident signal, $s(t) = [s_1(t)s_2(t)......s_K(t)]^T$, and the additive noise, $n(t)$, is expressed by the formula below

$$x_C(t) = C_R A(\theta,\phi)s(t) + n(t) \quad t = 1, 2, ...L \quad (1)$$

where C_R is the coupling matrix between sensor elements when the array is in use for a real measurement environment. This matrix has dimensions of $(M \times M)$, where M is the number of sensors. The steering vector matrix is : $A(\theta,\phi) = [a(\theta_1,\phi_1)......a(\theta_K,\phi_K)]$. The steering vector for the proposed array geometry is needed to compute the elevation angle (θ_k) and azimuth angle (ϕ_k); to achieve this, we define unit vectors that include θ_k and ϕ_k angles as follows:

$$u_k = cos\phi_k sin\theta_k \hat{a}_x + sin\phi_k sin\theta_k \hat{a}_y + cos\theta_k \hat{a}_z \quad (2)$$

where $\hat{a}_x$, $\hat{a}_y$, and $\hat{a}_z$ are unit vectors.

The vector, v_i, that represents the distance from the central point to the rest of the sensors can be defined as follows:

$$v_i = r_i cos\varphi_i \hat{a}_x + r_i sin\varphi_i \hat{a}_y, \quad i = 1, 2, \ldots, M. \quad (3)$$

where $\varphi_i = (2\pi/M)(i-1)$ is the angular separation. By utilizing the dot product between the v_i and u_k vectors, the angle, α_{ik} can be determined as follows:

$$\alpha_{ik} = cos^{-1}(sin\theta_k cos(\phi_k - \varphi_i)). \quad (4)$$

The plane wave time delay can be computed using the difference in distance (τ_{ik}) as presented below

$$\tau_{ik} = rcos\alpha_{ik} = rsin\theta_k cos(\phi_k - \varphi_i). \quad (5)$$

Now, one can calculate the phase difference (ψ_{ik}) as follows:

$$\psi_{ik} = \beta.\tau_{ik} = \frac{2\pi}{\lambda}rsin\theta_k cos(\phi_k - \varphi_i). \quad (6)$$

Then, the steering vector of the proposed array is given by

$$a(\theta_k,\phi_k) = \begin{bmatrix} e^{-j\psi_{1k}} & e^{-j\psi_{2k}} & \ldots & \ldots & e^{-j\psi_{Mk}} \end{bmatrix}. \quad (7)$$

III. SENSOR DESIGN AND IMPLEMENTATION

Multielement low-profile antennas were first proposed in [33]: the height reduction in comparison with the traditional monopole antenna was achieved using four structures similar to the inverted F antenna (IFA) employing folded horizontal elements; the design produced a monopole-like radiation pattern. In this article, the idea presented in [33] was further extended using a logarithmic spiral design to maintain the low
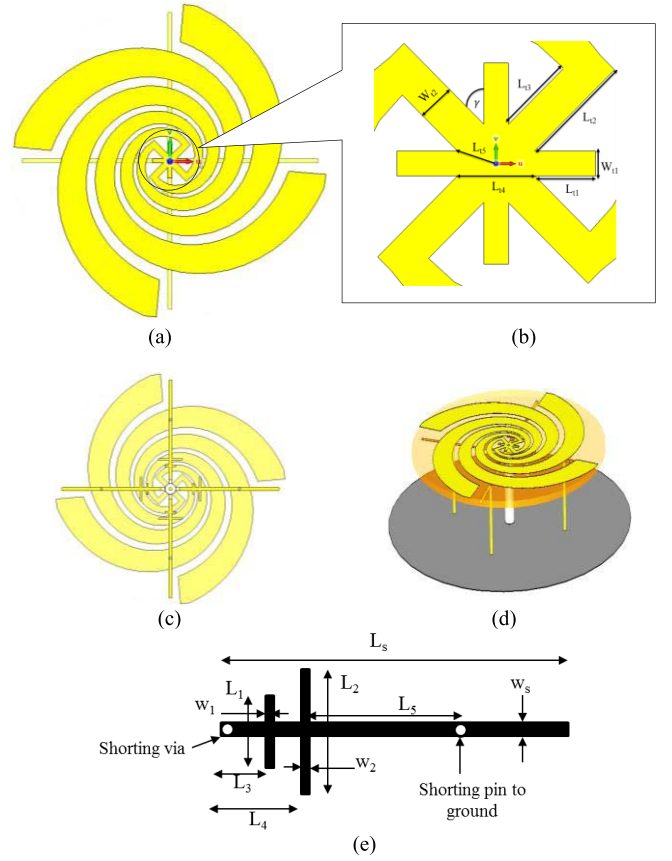

Fig. 2.   Model design of the proposed logarithmic spiral antenna. (a) Logarithmic spiral top layout. (b) Zoomed-in view of the stub with dimensional design details. (c) Bottom layout. (d) 3-D view of the spiral antenna. (e) One matching stub with dimensional design details.

profile and vertical polarization but with enhanced antenna bandwidth and dual-band ability. The Chu limit states that the fractional bandwidth depends on the size of the sensor and for applications requiring VHF/UHF bands; this presents a substantial challenge in terms of sensor design, in that it requires sufficient impedance bandwidth without increasing the overall sensor size. The proposed sensor was designed using a circular double-sided printed circuit board with a logarithmic layout on the top surface, as shown in Fig. 2(a), to obtain the best possible bandwidth under small size conditions.

The logarithmic spiral is preferred as this geometry usually provides better bandwidth than thin strip square spirals. The physical realization of the sensor structure used a Rogers Corp. FR-4 substrate with a thickness of 1.16 mm, a dielectric constant ε_r of 4.3, and a loss tangent of 0.02. The multiarm log-spiral had four spirals and they were printed on the top of the substrate with a radius of 6 mm. Each spiral has 1.12 turns and the progression factor is 0.26 with a 5° increment angle. These spirals serve as the horizontal elements, analogous to those of the folded monopole. The other parameters of the design of the top layout are shown in Fig. 2(b) while their values are given in Table I. Due to the small size of the antenna, a matching circuit was added on the underside of the substrate of the log-spirals, designed to give an adequate bandwidth. The matching stubs and feeding point are illustrated in Fig. 2(c). There are four shorting vias and four shorting pins, as depicted in Fig. 2(d).

TABLE I
SHOWING THE DESIGNED PARAMETERS OF THE STUB CIRCUIT

Parameter	Value (mm)
L_{t1}	2.4
L_{t2}	4.54
L_{t3}	3.2
L_{t4}	3.12
L_{t5}	1.64
W_{t1}	1
W_{t2}	1.5
γ	45°

TABLE II
SHOWING THE DESIGNED PARAMETERS OF THE MATCHING CIRCUIT

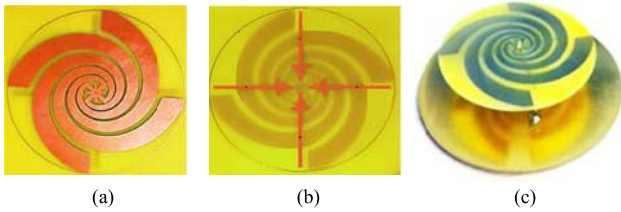| Parameter	Value (mm)
Ls	31
Ws	1
L_1	3.5
L_2	7.5
L_3	4
L_4	6
L_5	18.6
$W_1 = W_2$	0.5

Fig. 3. Fabricated log-spiral antenna of (a) top layer, (b) bottom layer, and (c) 3-D printed antenna.
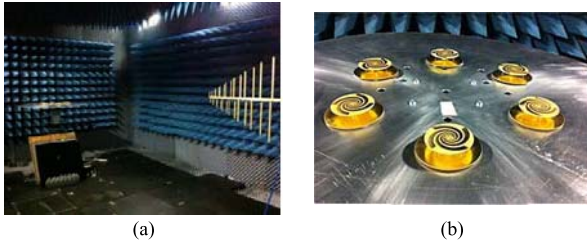

Fig. 4. Testing the proposed antenna array. (a) Measurement setup. (b) Zoomed-in view of the prototype receiver antenna array.

The shorting vias are used to connect the logarithmic spirals to the matching circuit through the upper substrate: they have a cylindrical shape with a length 1.6 mm and radius 1 mm. The shorting pins are used to connect the matching circuit to the ground plane through wire cylinders with height 16.4 mm (i.e., the height from the radiating layer to the ground plane). The structure of the matching stubs is depicted in Fig. 2(e). The dimensional parameters are given in Table II, and were computed and optimized to perform appropriately at the required resonant frequencies. Based on these optimized design parameters, six examples of the multiarm logarithmic spiral antenna were fabricated, as illustrated in Fig. 3. The sensor array geometry proposed in Fig. 1 was installed and tested in an anechoic chamber, as shown in Fig. 4. The simulated and measured return loss (i.e., S_{11}) for one of these sensors over the two bands, with the other sensors matched at 50 Ω, is shown in Fig. 5.
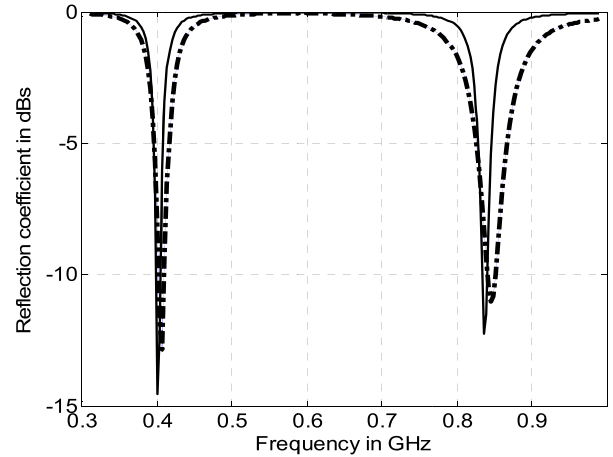

Fig. 5. Input reflection coefficient. Simulated, solid line; measured, dashed line.
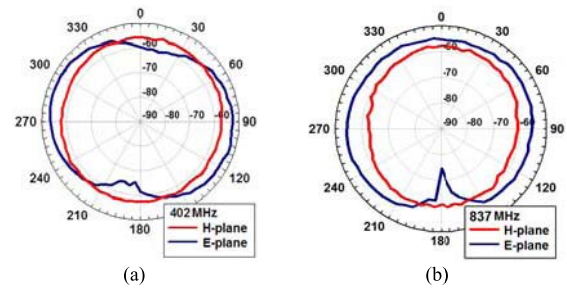

Fig. 6. Measured received signal (dBm) of (a) 402 and (b) 837 MHz.

For the lower band, the spectrum bandwidth at -10 dB reflection coefficient is 5 MHz, which is equivalent to 1.24% fractional bandwidth. For the higher band, the obtained bandwidth is 12 MHz, equivalent to 1.43% fractional bandwidth. Generally, there is a good agreement between the simulated and measured reflection coefficients over the lower band. Across the upper band, the agreement is less good, but the measured result shows somewhat wider bandwidth, possibly due to losses.

Looking carefully at the received power distribution, it is seen that the antenna is vertically polarized in the H-plane (i.e., the *xy* principal plane cut) as shown in Fig. 6, whereas the E-plane corresponds to the *xz* or *yz* planes. The asymmetry of the E-plane pattern is probably due to some imperfection of alignment during the measurement. Additionally, the appearance of a weak null could be due to the ground plane not being large enough. Clearly, the antenna element exhibits omnidirectional radiation in both frequency bands. Due to the small size of the element, the design concept of the proposed antenna array is appropriate for integration with an RF front end for tracking-system applications.

A. Decoupling Method

MC represents self-interferences between the antenna array elements in which undesired addition of magnitude and phase errors of the independent received signals for a given antenna element will occur. This will deteriorate the performance of the direction-finding method. Depending on the MC strength, its effect sometimes influences the performance of the receiving array critically because the MC between the antenna array elements will invalidate the initial calibration of the array

steering vector. The impact of MC can be analyzed by calculating the mutual impedances between the array radiators [34]. To remove such effects, the mutual impedances in receiving mode under an external plane-wave excitation condition have been computed. To this end, consider the antenna elements terminated with a known load impedance (Z_L). Also, consider an antenna array consisting of M sensors, each one of them terminated with an identical Z_L. The mutual interaction matrix can be measured as follows.

The voltage induced in one of the antenna elements, based on its coupling with other antenna elements, can be defined as follows:

$$V_k = I_1 Z_t^{k,1} + I_2 Z_t^{k,2}$$
$$+ \cdots + I_{k-1} Z_t^{k,k-1} + I_{k+1} Z_t^{k,k+1} + \cdots + I_M Z_t^{k,M} \quad (8)$$

where I_i is the induced current at the antenna element terminal while $Z_t^{k,i}$ is the receiving mutual impedance between antenna elements k and i. The subscript t refers to the impedance of receiving mutual mode at the antenna's terminals. It should be noted that for $k = i$, the impedance coupling is equal to Z_L. It is obvious that the computation of the receiving mutual impedances depends only on the terminal voltages or currents. Since the proposed antenna has an omnidirectional radiation pattern, it may be presumed that the distribution of current remains constant regardless of the direction of the impinging signal and, consequently, the impedance of the receiving element should remain unchanged [35]. To compute the mutual impedances, two antenna elements of the array need to be considered at each time while the other elements remain loaded. The following steps have been applied to obtain the corresponding C_{ik} parameters:

Step 1: Measure the mutual impedance at the first end "C_{12_1}" under the condition that the second element is connected to the load.

Step 2: Measure the mutual impedance at second terminal "C_{12_2}" while the first element is connected to the load.

Step 3: Measure the mutual impedance at the first end "C'_{12_1}," subject to removal of the second sensor from the array.

Step 4: Measure the mutual impedance at the second terminal "C'_{12_2}," under the condition that the first sensor is taken out of the array.

After measuring the above parameters, the receiving mutual impedances can be obtained as follows:

$$Z_t^{12} = \frac{C_{12\_1} - C'_{12\_1}}{C_{12\_2}} Z_0 \quad (9)$$

$$Z_t^{21} = \frac{C_{12\_2} - C'_{12\_2}}{C_{12\_1}} Z_0. \quad (10)$$

The above steps need to be repeated for all pairs of sensors in the antenna array to measure the total MC matrix C_M as follows:

$$C_M = \begin{bmatrix} 1 & -\dfrac{Z_t^{12}}{Z_L} & \cdots & -\dfrac{Z_t^{1M}}{Z_L} \\ -\dfrac{Z_t^{21}}{Z_L} & 1 & \cdots & -\dfrac{Z_t^{2M}}{Z_L} \\ \vdots & \vdots & \ddots & \vdots \\ -\dfrac{Z_t^{M1}}{Z_L} & -\dfrac{Z_t^{M2}}{Z_L} & \cdots & 1 \end{bmatrix} \quad (11)$$
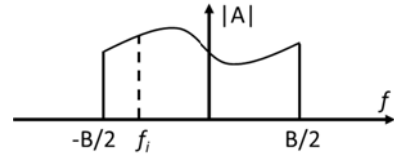

Fig. 7. Assumed bandwidth range.

where C_M represents the total measured MC with M $\times$ M size. Now, the uncoupled voltage vector $x(t)$ can be achieved as follows:

$$x(t) = \begin{bmatrix} x_1(t) \\ x_2(t) \\ \vdots \\ x_M(t) \end{bmatrix} = C_M^{-1} x_C(t)^T = C_M^{-1} \begin{bmatrix} x_{C1}(t) \\ x_{C2}(t) \\ \vdots \\ x_{CM}(t) \end{bmatrix}. \quad (12)$$

IV. OFDM SCHEME MODELING

The OFDM scheme can provide many more suitable solutions than a single-carrier modulation scheme. Thus, it is used here to enhance the flat fading of narrow multicarrier modulation over a broadband spectrum and to overcome the problems associated with multipath effects within the propagation channel. The narrower time resolution and the higher number of array elements make it easier to estimate the true angles of arrival [36]. To describe the methodology of the multicarrier system, consider the impulse response channel defined as follows:

$$h(\tau) = \sum_{k=1}^{n} b_k e^{j\Phi_k} \delta(t - \tau_k) \quad (13)$$

where b_k is the amplitude of the path signal, Φ_k represents the phase of the incident path, τ_k is the time delay in receiving each path, and n is the total number of received paths. An input signal $f(t, \omega) = e^{j\omega t}$ is then applied to this and the output can be simplified to the following:

$$s(t, \omega) = e^{j\omega t} \sum_{k=1}^{n} b_k e^{j\Phi_k} e^{j\omega \tau_k} = e^{j\omega t} U(\omega). \quad (14)$$

Extending $U(\omega)$ over a suitable bandwidth, B (as depicted in Fig. 7) for N subcarrier frequencies, the ith frequency sample can be expressed by

$$f_i = -\frac{B}{2} + (i-1)\frac{B}{N-1} \quad \text{for } i = 1, 2 \ldots \ldots N. \quad (15)$$

Here

$$\Delta f = \frac{B}{N-1}. \quad (16)$$

The sampling interval may be stated as follows:

$$\frac{1}{2\Delta t} = \frac{B}{2} \implies \Delta t = \frac{1}{B}. \quad (17)$$

Therefore, the minimum frequency of sampling should be

$$f_s \geq 2 \times \frac{B}{2}. \quad (18)$$

The ith uniform frequency sample of $U(\omega)$ can be given by

$$U(2\pi f_i) = \sum_{k=1}^{n} b_k e^{j\Phi_k} e^{-j\omega \tau_k} e^{-j2\pi f_i \tau_k}. \quad (19)$$

It should be noted that the above frequency-domain equation will represent the received signal at the output port of the mth sensor and this is simply equivalent to

$$x_m(f) = S_m(\omega).H_m(\omega) = \{U(2\pi f_i)\}. \tag{20}$$

If thermal noise is added to the received signal, then by applying the inverse fast Fourier transform (IFFT), the signal in the time domain, $x_m(t)$, can be expressed as follows:

$$x_m(t) = IFFT(S(\omega).H(\omega)) + n(t). \tag{21}$$

This signal will be used in Section V to extract the AOAs. The average delay spread for each received element was computed over several scenarios of multiple carriers and found to be between 0.5 and 1.5 μs. Thus, the coherence bandwidth utilized for such values is between 0.66 and 2 MHz. The OFDM signal was implemented over a wide bandwidth of 5 MHz and therefore, it can be assumed that a frequency selective channel has been created, based on the values of the coherence bandwidth. Further, based on the range of the OFDM signal bandwidth, AOA estimation can be applied using several criteria, for example, greatest carrier strength (i.e., the highest power level of the subcarrier in the OFDM), least TOA (i.e., the TOA of the first subcarrier), and the averaging of all, or a small number, of received paths to estimate the AOA (for example, the average over the first ten subcarriers).

V. PV Algorithm Based on the OFDM Scheme

For a wide bandwidth wireless transmission, the spectral response of the channel is not flat. The spectral response could be affected by fading and may contain nulls that are caused by the characteristics of the propagation channel. This might mean that certain frequencies could be strongly attenuated at the receiver and may present deep fades in the RSS if they arrive at the receiver with the same power as that of the direct LOS path and then destructively interfere [36], [37]. With a narrowband transmission system, the signal can be entirely lost if a null is present in the frequency response at the transmit frequency.

However, with a wideband AOA system, a complete loss of the received signal can be avoided through splitting the transmission bandwidth into many small narrowband carriers using OFDM [38]. In such a transmission scheme, multiple carrier frequencies can be used to encode the data digitally. This results in the transformation of the frequency-selective channel into several flat-fading channels. Any loss of data can be prevented using coded OFDM in which forward error correction (FEC) codes can be applied to the signal before transmission [38], [39]. Another challenge arises as a result of the received signal paths arriving at the receiver with associated delays due to the difference in the path length traveled and the received energy spreads in time: this is referred to as channel delay spread. The channel delay spread can be described as the time between the first and the last significant multipath signals arriving at the receiver [38]. This delay spread is responsible for intersymbol interference (ISI) in digital wireless communications: this occurs when a delayed multipath signal overlaps the following symbols. One method to reduce ISI is to divide the bandwidth into several subchannels using OFDM.

To overcome the challenges mentioned above, a low complexity and high-accuracy AOA estimation algorithm based on a single snapshot is proposed and integrated with the OFDM modulation scheme to localize an unknown object. This algorithm computes the cross correlation vector (CCV) between the measured signal in the first antenna element and the rest of the elements. Consequently, the PV method can directly find the directions of the incident paths from the observation matrix, avoiding the correlation matrix calculations. To model this algorithm, suppose a single snapshot of data is collected at M receivers; the measured data vector is passed to the OFDM modulation scheme. The observed data can be described below

$$x_m(t) = \begin{bmatrix} x_1(t) & x_2(t) & \cdots & \cdots & x_M(t) \end{bmatrix}. \tag{22}$$

Divide $x_m(t)$ into two subvectors as follows:

$$q_1 = [x_1(t)] \tag{23}$$
$$q_2 = \begin{bmatrix} x_2(t) & x_3(t) & \cdots & \cdots & x_M(t) \end{bmatrix} \tag{24}$$

where q_1 represents the measured data at the first sensor element while q_2 contains the data obtained from the rest of the elements. Now, compute the propagator vector as follows:

$$p = q_1 q_2 \tag{25}$$

here, p denotes the CCV of the time series from the first antenna element with the rest of the antenna elements. This has the effect of normalizing to the first antenna's phase and eliminating the dependence on the time series of the signal. Consequently, p assimilates all the data about how the phasors of the incoming signals from different angles sum at every antenna element. It also reduces the dependence on the steering vectors and hence extracts the incoming angles efficiently. This, in turn, enhances immunity to noise, and therefore, the AOAs can be found efficiently with a single (or small number of) data measurement/s and/or poor signal-to-noise ratios (SNRs). The autocorrelation of the first element with itself, $\hbar = x_1(t)x_1(t)$ was added since the size of p is $1 \times (M-1)$; this yields

$$v = \begin{bmatrix} \hbar & p \end{bmatrix}. \tag{26}$$

It is essential to compute p based on the measured signal in the first antenna element and the rest of the elements since any reduction in the number of the "rest elements" will minimize the effective aperture size of the antenna array and consequently decrease the AOA estimation accuracy. The pseudospectrum can be constructed as follows:

$$P(\theta_k, \phi_k) = |va^H|^2. \tag{27}$$

For simplicity, $A(\theta, \phi)$ and $a(\theta, \theta)$ will be written in the rest of the manuscript as A and a, respectively.

To eliminate the sidelobes and extract the real peaks efficiently, first the spatial spectrum of the above formula is normalized thus

$$P_{Norm}(\theta_k, \phi_k) = P(\theta_k, \phi_k)/max(P(\theta_k, \phi_k)). \tag{28}$$

Next, subtract $P_{Norm}(\theta_k, \phi_k)$ from unity as follows:

$$P_S(\theta_k, \phi_k) = 1 - P_{Norm}(\theta_k, \phi_k). \tag{29}$$

The final equation that is used to determine the arrival angles then becomes

$$P_{PV}(\theta_k, \phi_k) = \frac{1}{P_S(\theta_k, \phi_k) + \varepsilon}. \tag{30}$$

Here, ε is a small scalar value inserted to overcome the potential singularities that may occur due to the subtraction and inversion processes in the pseudospectrum

construction stage. It is set as $\varepsilon = 0.01$ so that genuine peaks can be exaggerated: these indicate the actual AOAs and suppress the side lobes and false peaks. It can be seen that the PV algorithm can find the arrival angles with a low-computational burden. The computational complexity of this method is analyzed and compared with several popular direction-finding techniques in Section V-B.

A. Cramer–Rao Lower Boundary of the PV Method

Typically, Cramer–Rao lower boundary (CRLB) is an efficient tool that can be used to measure the performance of any unbiased DOA estimator: it computes the physical impossibility of the variance being less than the bound [40]. In other words, the CRLB represents the statistical lower bound of the mean-square error between an estimator and its actual value [41], [42]. Thus, the CRLB of the PV method is derived and used as an optimality criterion for the parameter estimation problem. It is calculated from the probability-likelihood function of the received signal, where the received signal is modeled as a complex Gaussian random variable with a deterministic mean to include both weak and strong scattering [43], [44]. From (26), the PV can be presented here as follows:

$$\boldsymbol{v}(t) = \begin{bmatrix} \hbar & \boldsymbol{p} \end{bmatrix} = [x_1(t) \; x_1(t) \; x_1(t) \; \{x_2(t) \cdots x_M(t)\}]$$
$$\boldsymbol{v}(t) = x_1(t)\begin{bmatrix} x_1(t) \cdots\cdots x_M(t) \end{bmatrix} = x_1(t)\boldsymbol{x}(t).$$

By assuming the received signal, $\boldsymbol{x}(t)$, contains both additive white Gaussian noise (AWGN) and color noises, $\boldsymbol{v}(t)$ becomes as follows:

$$\boldsymbol{v}(t) = x_1(t)\{\boldsymbol{A}\boldsymbol{s}(t) + \boldsymbol{e}(t)\}$$
$$\boldsymbol{e}(t) = \boldsymbol{\mathcal{G}}(t) - \boldsymbol{A}\boldsymbol{s}(t) \tag{31}$$

where $\boldsymbol{\mathcal{G}}(t) = (v(t)/x_1(t))$, $e(t) = n(t)+m(t)$, and $m(t)$ is the non-Gaussian or color noise. The probability density function (PDF) of the Gaussian and non-Gaussian noise can be given as follows:

$$f(\boldsymbol{n}_i(t)) = f(\bar{\boldsymbol{n}}_i(t)) f(\tilde{\boldsymbol{n}}_i(t)) \tag{32}$$
$$f(\boldsymbol{m}_i(t)) = f(\bar{\boldsymbol{m}}_i(t)) f(\tilde{\boldsymbol{m}}_i(t)). \tag{33}$$

Parametric techniques are used to evaluate the Gaussian noise distributions. One can use a kernel or Laplace method to estimate the PDF of non-Gaussian noise [45], [46]. The CRLB matrix is defined as the inverse of the Fisher information matrix (FIM) [47]

$$\text{CRLB} = \boldsymbol{J}^{-1}. \tag{34}$$

The FIM is given as follows [48]:

$$\boldsymbol{J} = E\left[\frac{\partial \ln f(\boldsymbol{v}|\boldsymbol{\psi})}{\partial \boldsymbol{\psi}}\left(\frac{\partial \ln f(\boldsymbol{v}|\boldsymbol{\psi})}{\partial \boldsymbol{\psi}}\right)^T\right]. \tag{35}$$

Here, $\boldsymbol{\psi}$ is a vector of the unknown parameters and defined as follows [49]:

$$\boldsymbol{\psi} = [\sigma^2 \bar{s}(1)^T \tilde{s}(1)^T \cdots \cdots \bar{s}(L)^T \tilde{s}(L)^T \; \theta^T]^T. \tag{36}$$

For an unbiased AOA estimator, the following condition needs to be satisfied:

$$E\left[(\hat{\boldsymbol{\psi}}-\boldsymbol{\psi})(\hat{\boldsymbol{\psi}}-\boldsymbol{\psi})^T\right] \geq \text{CRLB} \tag{37}$$

where $\hat{\boldsymbol{\psi}}$ is an estimate of $\boldsymbol{\psi}$. It can be seen from (37) that the CRLB gives the best achievable estimation resolution for an unbiased AOA estimator. The PDF of the real part of the Gaussian noise can be written as follows:

$$f_{\bar{n}i}(\bar{n}i(t)) = \frac{1}{\sqrt{2\pi}\sigma/2} e^{-\left(\frac{\bar{n}i(t)^2}{\sigma^2}\right)}. \tag{38}$$

While the PDF of the real part of the non-Gaussian noise can be defined as follows:

$$f_{\bar{m}_i}(\bar{m}_i(t)) = \frac{1}{\sqrt{2\pi}T\bar{\varrho}^2} \sum_{j=1}^{T} e^{-\left(\frac{(\bar{m}_i(t)-\bar{m}_j)^2}{2\bar{\varrho}^2}\right)}. \tag{39}$$

Then, the PDF of the real part of the mixed noise $\bar{n}i(t)$ and $\bar{m}i(t)$ is given below

$$f_{\bar{e}_i}(\bar{e}_i(t)) = \frac{\sum_{j=1}^{T} e^{-\left(\frac{(\bar{e}_i(t)-\bar{m}_j)^2}{2\left(\frac{\sigma^2}{2}+\bar{\varrho}^2\right)}\right)}}{T\sqrt{2\pi\left(\frac{\sigma^2}{2}+\bar{\varrho}^2\right)}}. \tag{40}$$

The PDF of the total mixed noise, including the real and imaginary parts is given as follows:

$$f_{e_i}(e_i(t)) = f_{\bar{e}_i}(\bar{e}_i(t)) f_{\tilde{e}_i}(\tilde{e}_i(t))$$
$$= \mathcal{M} \sum_{j=1}^{T} e^{-\bar{\mathcal{U}}} \sum_{j=1}^{T} e^{-\tilde{\mathcal{U}}} \tag{41}$$

where $\mathcal{M} = (1/2\pi T^2 \sqrt{\left(\frac{\sigma^2}{2}+\bar{\varrho}^2\right)\left(\frac{\sigma^2}{2}+\tilde{\varrho}^2\right)})$, T denotes the number of survey set, $\bar{\mathcal{U}} = ((\bar{e}_i(t)-\bar{m}_j)^2)/(2\left(\frac{\sigma^2}{2}+\bar{\varrho}^2\right))$, and $\tilde{\mathcal{U}} = ((\tilde{e}_i(t)-\tilde{m}_j)^2)/(2\left(\frac{\sigma^2}{2}+\tilde{\varrho}^2\right))$.

The PDF of the $f(e_i(t))$ can be obtained by substituting (31) in (41), yielding

$$f(v_i(t)) = \mathcal{M} \sum_{j=1}^{T} e^{-\left(\frac{\left(\bar{\boldsymbol{\mathcal{G}}}_i(t)-\sum_{k=1}^{K}(\bar{A}_{ik}\bar{s}_k(t)-\tilde{A}_{ik}\tilde{s}_k(t))-\bar{m}_j\right)^2}{2\left(\frac{\sigma^2}{2}+\bar{\varrho}^2\right)}\right)}$$
$$\times \sum_{j=1}^{T} e^{-\left(\frac{\left(\tilde{\boldsymbol{\mathcal{G}}}_i(t)-\sum_{k=1}^{K}(\bar{A}_{ik}\bar{s}_k(t)+\tilde{A}_{ik}\tilde{s}_k(t))-\bar{m}_j\right)^2}{2\left(\frac{\sigma^2}{2}+\tilde{\varrho}^2\right)}\right)}. \tag{42}$$

The joint PDF $f(\boldsymbol{v}|\boldsymbol{\psi})$ can be given as follows:

$$f(\boldsymbol{v}|\boldsymbol{\psi}) = \prod_{t=1}^{L}\prod_{i=1}^{M} f(v_i(t)). \tag{43}$$

By taking the partial derivative of (43), this yields

$$\frac{\partial \ln f(\boldsymbol{v}|\boldsymbol{\psi})}{\partial \boldsymbol{\psi}} = \sum_{t=1}^{L}\sum_{i=1}^{M} \frac{1}{f(v_i(t))} \frac{\partial \ln f(v_i(t))}{\partial \boldsymbol{\psi}}. \tag{44}$$

Now, we substitute (44) into (35), giving

$$J_{mn} = E \left\{ \frac{\sum_{t_1=1}^{L} \sum_{i_1=1}^{M} \sum_{t_2=1}^{L} \sum_{i_2=1}^{M} \frac{1}{f(v_{i1}(t_1))} \frac{1}{f(v_{i2}(t_2))}}{\frac{\partial f(v_{i1}(t_1))}{\partial \psi_m} \frac{\partial f(v_{i2}(t_2))}{\partial \psi_n}} \right\}. \quad (45)$$

It should be noted that all the terms for $t_1 \neq t_2$ and $i_1 \neq i_2$ are equal to zero [43] and, thus (45) becomes

$$J_{mn} = E \left\{ \sum_{t=1}^{L} \sum_{i=1}^{M} \frac{1}{f(v_i(t))^2} \frac{\partial f(v_i(t))}{\partial \psi_m} \frac{\partial f(v_i(t))}{\partial \psi_n} \right\}. \quad (46)$$

By substituting (46) into (35), we obtain

$$J = \begin{bmatrix} \xi & 0 & \cdots & 0 & 0 \\ 0 & G & \cdots & 0 & \Delta_1 \\ \vdots & \vdots & \ddots & \vdots & \vdots \\ 0 & 0 & \cdots & G & \Delta_L \\ 0 & \Delta_T^1 & \cdots & \Delta_L^T & \Upsilon \end{bmatrix}. \quad (47)$$

Here, $\xi = (\sigma^2/ML)$ [43], whereas the other parameters of the J matrix are derived and defined as given in Appendix A. Now, the CRLB can be found by substituting (47) into (34), yielding

$$CRLB(\theta) = \left\{ \Upsilon - \left[\Delta_1^T \ldots \Delta_L^T \right] \begin{bmatrix} G^{-1} & \cdots & 0 \\ \vdots & \ddots & \vdots \\ 0 & \cdots & G^{-1} \end{bmatrix} \begin{bmatrix} \Delta_1 \\ \vdots \\ \Delta_L \end{bmatrix} \right\}^{-1}.$$

The above equation can be simplified as follows:

$$CRLB(\theta) = \left(\Upsilon - \sum_{t=1}^{L} \Delta_t^T G^{-1} \Delta_t \right)^{-1}. \quad (48)$$

Then, the lowest estimation error of the PV method under the CRLB criterion can be obtained as follows:

$$PV_{CRLB} = \frac{1}{K} trace\{CRLB(\theta)\}. \quad (49)$$

B. Complexity Analysis

The complexity of localization systems describes the complexity of the software, hardware, and operating components that are needed to establish any localization system and thus it is important to consider them. The execution time is also an essential factor in any application: this should desirably be as small as possible. Typically, three main stages can be considered to measure the complexity of the AOA method, as follows:

1) Construction of the covariance matrix.
2) Applying eigenvalue decomposition (EVD), computing matrix inversion, or the projection matrix/vector.
3) Decide the scanning angle step to form a pseudo spectrum.

In addition, some AOA methods need to know the number of arriving signals in advance, which is not possible in the practical applications. Consequently, one needs to apply a preprocessing signal stage to determine the arrival signals' number. The computational operations required to construct the covariance matrix are $O(M^2L)$, where M is the number of antenna elements and L is the number of snapshots. In contrast, the arithmetic operations needed to compute the propagator vector (v) are $O(M)$. Further, if applying EVD or computing the inversion of the covariance matrix, the required operations

TABLE III
COMPUTATIONAL OPERATIONS COMPARISON BETWEEN THE PV AND OTHER AOA ALGORITHMS

Algorithm	The needed computational operations
Capon [50]	$O(M^2L + M^3 + M^2 J_\theta J_\phi)$
Min-Norm [51]	$O(M^2L + M^3 + M J_\theta J_\phi)$
MUSIC [52]	$O(M^2L + M^3 + M^2 J_\theta J_\phi)$
Propagator [53]	$O(M^2L + M^2K + M^2 J_\theta J_\phi)$
AV [54]	$O(M^2L + M^2K J_\theta J_\phi)$
CG [55]	$O(M^2L + M^2 K J_\theta J_\phi)$
OGSBI [56]	$O(M^2L + \max(M(J_\theta J_\phi)^2, ML J_\theta J_\phi))$ per iteration
Root SBL [57]	$O(M^2L + M J_\theta J_\phi)$ per iteration
PV	$O(ML + M J_\theta J_\phi)$

are approximately $O(M^3)$. However, there is no need for these operations with the PV method.

Finally, the computational operations required to form a spatial spectrum are dependent on two factors, namely: the dimension of the matrix used and the scanning angle step. The former is based on the value of M and the applied AOA method. The latter can be determined in the following way: suppose δ_θ and δ_ϕ represent the scanning angle steps for the elevation and azimuth planes, respectively, then the total operation numbers for these planes are $J_\theta = 90°/\delta_\theta$ and $J_\phi = 360°/\delta_\phi$, respectively. Based on the above arguments, the computational complexity of this method may be compared with several common AOA algorithms, as shown in Table III.

As can be seen from this table, the PV algorithm can find the arrival angles with the lowest complexity, making processing more efficient than with the other methods.

VI. NUMERICAL SIMULATIONS AND DISCUSSION

Localization and tracking of unknown objects based on a single snapshot/measurement is a vital consideration since large numbers of measurements are not continuously obtainable in wireless communication systems, especially when the tracked objectives are changing rapidly. To justify the theoretical claims of the proposed system, three main scenarios were implemented. The first scenario was to track a nonstationary object for public security applications. The second was an outdoor-to-outdoor tracking scenario, and outdoor-to-indoor localization was investigated in the last scenario, as would be relevant for search-and-rescue operations. The MATLAB software was used to evaluate the performance of the PV method and compare it with other AOA algorithms; multipath propagation and NLOS data of the agents' positions and vehicle movements were established using the Wireless-InSite software, while CST Microwave Studio software was used to design and model the spiral sensor.

A. Tracking a Nonstationary Object

In this test, the performance of the proposed system was evaluated when estimating the direction of a movable object for tracking applications. As the tracked object moves from one place to another, its corresponding direction changes as well. Therefore, it is necessary to estimate the direction of this object adaptively. The tracked object was assumed to travel in a zigzag route; the total travel distance being 6 km. The proposed six-element spiral antenna array was considered as used to find the direction of this object using only a single
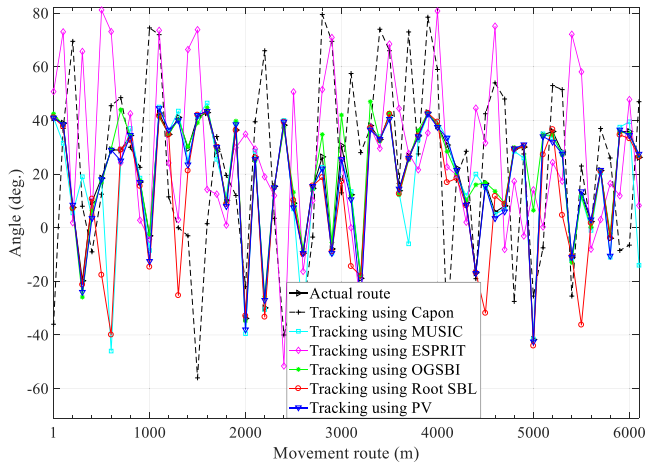
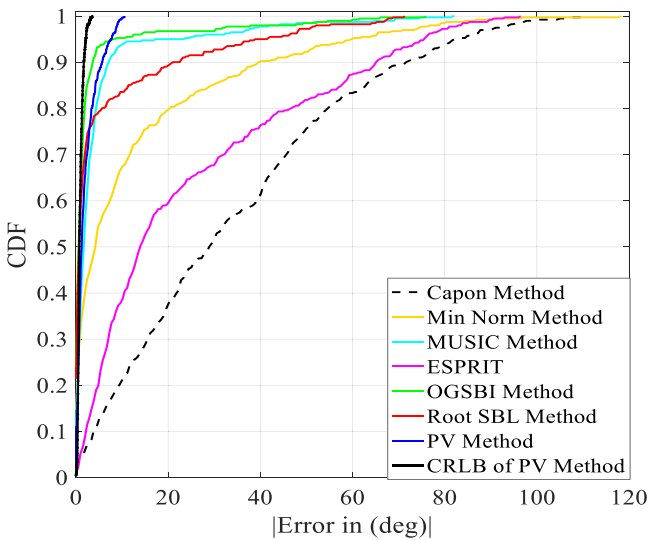Fig. 8.   Tracking performance comparison with various AOA methods.

Fig. 9.   Estimation error comparison during the tracking process.

snapshot with an SNR of 3 dB. At each 200 m, a measurement was taken to determine the direction of the movement toward the tracked object.

The performance of the PV method within the proposed scheme was compared with several well-known AOA methods, as shown in Fig. 8. It can be clearly seen that the Capon and ESPRIT algorithms mostly failed to track the moveable object, whereas the MUltiple SIgnal Classification (MUSIC) and Root sparse Bayesian learning (SBL) methods gave better performance estimation. Although the off-grid sparse Bayesian inference (OGSBI) algorithm provided good tracking estimation, it failed during some points of the tracking process, namely at the 4.4 and 5 km points, with an error up to 50°. It is clear that the PV method gave the best tracking accuracy among the methods considered and it made the receiver travel in the correct path during the whole tracking route. In addition, it has low-computational complexity, as presented in Table III.

To provide an intensive and robust comparison, the same scenario was repeated with a total traveled distance of 40 km. The same AOA methods, plus additionally the minimum norm method, were used to track the wanted object. At each movement step, the direction of the movable transmitter was estimated and then the absolute estimation error calculated: the results are shown in Fig. 9. The results obtained confirm that
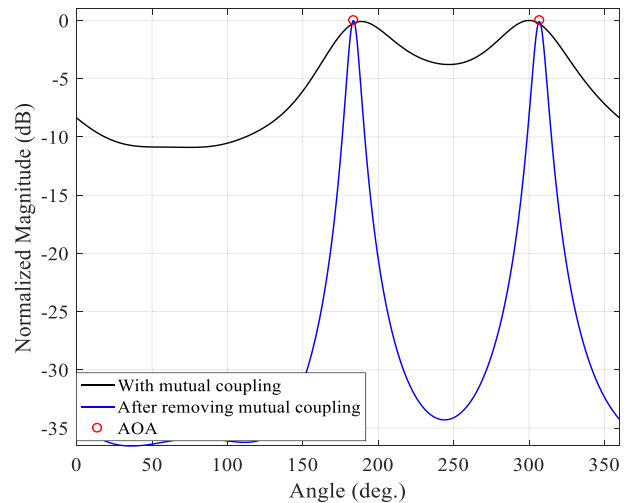

Fig. 10.   Performance of the PV method before and after removing the MC effect.

the PV method provides the best tracking estimation accuracy when compared with the other AOA methods under a single snapshot condition. It can be observed from this figure that the PV estimation error does not exceed 10° through the whole tracking scenario. The CRLB of the PV method shows the lowest estimation error that can be achieved using the PV method under this scenario conditions.

B. Impact of MC Within the Antenna Array on the AOA Estimation Accuracy

To show the MC effect on the estimation accuracy, the proposed spiral array combined with the PV method was assumed to be receiving two signals from different directions. The performance of the PV method under the MC effect is shown by the black line in Fig. 10, where the PV method has been applied to (1).

Although the PV method detected the directions of these two signal sources under MC influences, the two peaks produced are quite wide, with some deviation from the actual angles. However, the performance of the PV method after applying the decoupling approach to the measured data is shown by the blue line in Fig. 10. As illustrated, the PV method produced two sharp and accurate peaks in the directions of the arriving signals after applying the decoupling method [i.e., using (12)].

C. Outdoor-to-Outdoor Localization Scenario

This tracking scenario considered an urban environment in the city of Ottawa, Canada, as a model to test the tracking system performance. The six-element spiral antenna array was placed on top of a car, the height of the vehicle set to 1.5 m, and the car model available in the Wireless-InSite software was used, represented by conducting material only. The ground plane of the antenna array was separated from the top of the vehicle by 4 mm. In this scenario, only the lower frequency (f = 402 MHz) was considered, and therefore two triangles of elements were implemented as described in Section II. An urban area consists of many buildings of different materials and height levels: a maximum height of 50 m was used for the evaluation process, as shown in Fig. 11. An omnidirectional transmitting antenna was located at a height of 1.5 m and the
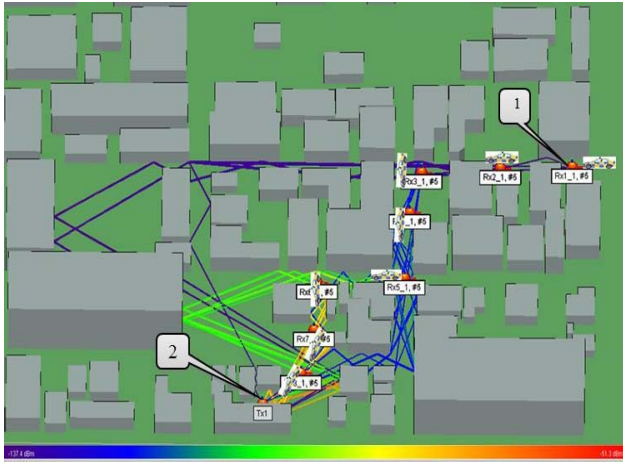
Fig. 11. Showing outdoor-to-outdoor tracking scenario; 1 is the starting point of the tracking process and 2 is the location of the hidden object.

Fig. 12. OFDM scheme using 32 subcarriers of the Tr_1 element set at the Rx1-1 point. (a), (c), and (e) Normalized power of the Tr_1 sensors while (b), (d), and (f) represent the corresponding phases for each element.

transmitting power level was set to 0.3 W (i.e., 24.78 dBm). With a single snapshot during the whole tracking process, the proposed sensor array was assumed to receive ten paths at each element, each having different power, TOA, and phase. However, due to obstructions, shadowing, and fading phenomena, the number of received paths could be less than ten.

A superposition theory approach was applied using the first and second triangular sets of elements, Tr1 and Tr2 and hence two different received data matrices were constructed, based on these triangles. To remove the coupling effects that can influence the estimation accuracy, a decoupling method was applied to compensate for such effects. In the urban area illustrated in Fig. 11, the received signal consists of multiple NLOS paths caused by reflections from the scatterers present in the propagation path between the transmitter and the receiver. Even when the LOS signal is available, a difficulty lies in the separation of the true LOS path from the delayed and overlapped replicas arriving at the receiver: the addition of noise further complicates the process. In addition, the multipath fading effects of the environment, such as Doppler shift signal attenuation, scattering, and low SNR make the process of detection of the signal source extremely difficult. All of these problems make it difficult to detect the LOS signal with absolute certainty.

To improve the signal source detection and obtain better resolution of the channel response in the time domain, a coded OFDM scheme was integrated with the proposed tracking system to mitigate the negative effects of multipath and improve the ability of the PV algorithm to resolve the received paths successfully. Therefore, the compensated data were passed to the OFDM scheme, where the modulation bandwidth was set to 5 MHz. This bandwidth was divided into 32 subcarriers, as illustrated in Fig. 12. The IFFT was then applied to the channel transfer function that was obtained to acquire the impulse response with arriving paths. After this, the impulse response data for each triangular set was passed to the PV method, where the decision of the movement from one place to another considered the computed angle based on four strategies. These strategies are the least TOA OFDM subcarrier, the strongest OFDM subcarrier, and the average of all (or some) of a selected number of OFDM subcarriers.

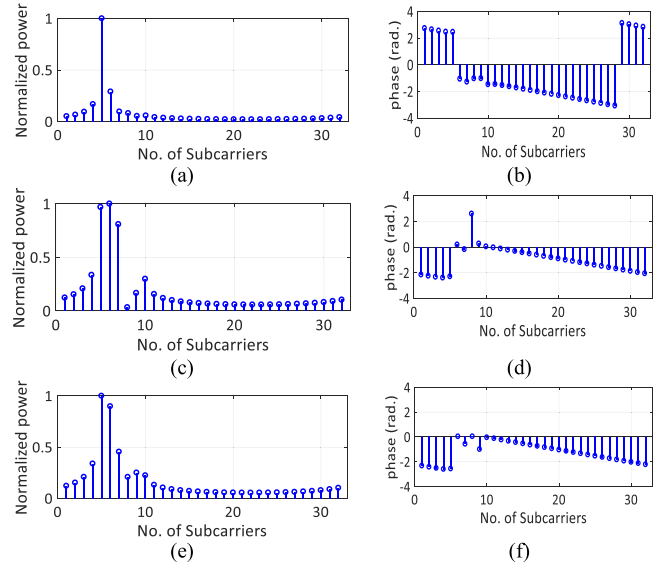The ultimate decision on the movement takes into account all the strategies mentioned above by computing the mean estimated angle ($\hat{\phi}_m$), defined in the equation below

$$\hat{\phi}_m = \frac{(\hat{\phi}_1 + \hat{\phi}_2 + \hat{\phi}_3 + \hat{\phi}_4)_{Tr1} + (\hat{\phi}_1 + \hat{\phi}_2 + \hat{\phi}_3 + \hat{\phi}_4)_{Tr2}}{8}.$$

Here, $\hat{\phi}_1$ is the estimated angle based on the least TOA OFDM subcarrier, $\hat{\phi}_2$ is the estimated angle based on the strongest OFDM subcarrier, $\hat{\phi}_3$ is the estimated angle based on the average of the strongest five OFDM subcarriers, and $\hat{\phi}_4$ is the estimated angle based on the average of all OFDM subcarriers. The scanning angle step was set at $\delta_\emptyset = 0.5°$ and $\varepsilon = 0.01$. The RSS method can be implemented on any wireless communication system without the need to change the hardware significantly. It can measure the average strength of incident signals from different paths at any given location. Thus, the RSS method was used as an extra tool to ensure that tracking was on the correct route, by reading the strength of the received paths at each move. The first measurement in the tracking process was taken at point Rx1-1 and then at point Rx2-1 and so on until the last point at Rx8-1. The car's position measurements at these points and the location of the hidden object are given in Table IV. At each measurement point, the estimated angles $\hat{\phi}_1$, $\hat{\phi}_2$, $\hat{\phi}_3$, and $\hat{\phi}_4$ based on both the Tr_1 and Tr_2 sets were computed, the results being presented in Table V. The mean estimated angle, $\hat{\phi}_m$, was calculated and presented in Table VI and then it was used as a final decision on the movement from one location to the other.

The RSS was measured at each position as presented in Table VI and compared with the previous reading just to ensure that the vehicle moved in the correct tracked route. At the Rx1-1 and Rx2-1 points, $\hat{\phi}_m$ is 186.24° and 203.62°, respectively, and therefore, the car moved toward the left direction, and another measurement was taken at the Rx3-1 point, as shown in Fig. 11. The measured RSS at this point compared to the previous two readings confirmed that the tracking process was proceeding in the correct route. The measured angle at Rx3-1, $\hat{\phi}_m$, was 271.74°, and thus, the direction of the car's movement was changed by 90° (i.e., it turned left), and it continued in the same direction until it reached point Rx5-1 since the measured angle at Rx4-1 was

TABLE IV

SHOWING THE SEQUENCE AND LOCATION OF THE RECEIVER AT EACH POINT IN THE TRACKING PROCESS IN ADDITION TO THE TRANSMITTER LOCATION

| Tracking steps sequences	Location of the receiver x (m)	Location of the receiver y (m)
a. Rx1-1	990	352
b. Rx2-1	910	349
c. Rx3-1	845	349
d. Rx4-1	842	269
e. Rx5-1	842	159
f. Rx6-1	771	157
g. Rx7-1	771	87
h. Rx8-1	749	40
i. Tx1	700	34

TABLE V

SHOWING THE ESTIMATED DIRECTION AT EACH MOVEMENT USING Tr_1 AND Tr_2 WITH SEVERAL CRITERIA

| Move No.		$\hat{\phi}_1$	$\hat{\phi}_2$	$\hat{\phi}_3$	$\hat{\phi}_4$
Rx1-1	Tr_1	186.5º	186º	185º	188º
	Tr_2	186.5º	185.5º	184.5º	188º
Rx2-1	Tr_1	192.5º	218.5º	192º	210.5º
	Tr_2	189.5º	220º	189º	217º
Rx3-1	Tr_1	272.5º	275.5º	272.5º	268º
	Tr_2	272.5 º	272º	272.5 º	268.5º
Rx4-1	Tr_1	269.5º	270º	269.5º	269º
	Tr_2	268.5º	269.5º	268.5º	268.5º
Rx5-1	Tr_1	203º	197º	202.5º	205º
	Tr_2	203.5º	217º	204º	217.5º
Rx6-1	Tr_1	259º	257º	248.5º	245.5º
	Tr_2	237.5º	244.5º	259º	241º
Rx7-1	Tr_1	230.5º	239º	231º	234º
	Tr_2	230.5º	239º	231º	233.5º
Rx8-1	Tr_1	184º	184º	184.5º	187º
	Tr_2	184.5º	184.5º	185º	187.5º

269.12°. The mean estimated angle at the Rx5-1 point was 206.18° and, hence, the direction of movement was turned right, as shown in Fig. 11. A new measurement was taken at the point Rx6-1 and the measured angles indicate that the movement direction needed to be turned left, as given in Fig. 13 and Table VI.

The reasons for the deviation of the results at the measured points Rx5-1 and Rx6-1 are that the arrival paths come from two different main routes ($\phi = 180°$ and $270°$) while the receiver subarrays consist of only three elements. Moreover, by assuming one element from each subarray as a reference, then, only two elements are left to compute the time delay. Consequently, due to the size of the subarrays being small, relatively high deviations in the obtained results can occur at those two measured points. To overcome this issue, we need to increase the number of antenna elements, for example, use 8, 10, or 12 elements, where two squares, pentagons, or hexagons are constructed, respectively, for the lower band.

However, size, hardware implementation, and computational complexity will increase significantly. Another new measurement was taken at point Rx7-1, where the direction was slightly changed toward the right to find the hidden object. Lastly, all the measured angles at the point Rx8-1, based on several strategies, indicated the location of the hidden object accurately, as given in Table V. It is also clear from this table that the measured RSS during the tracking steps showed that
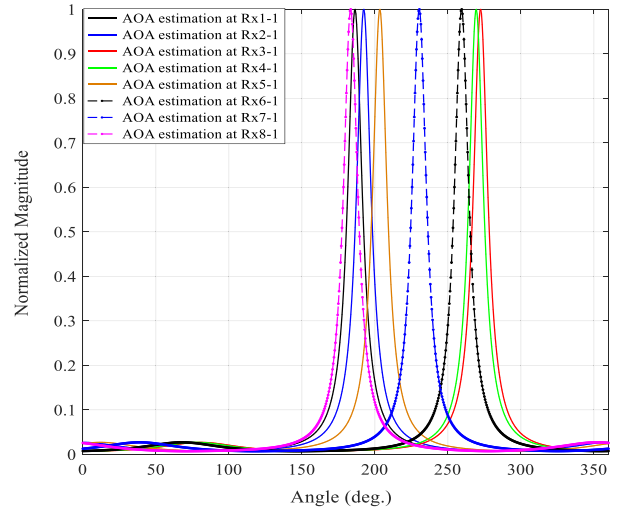
(a)
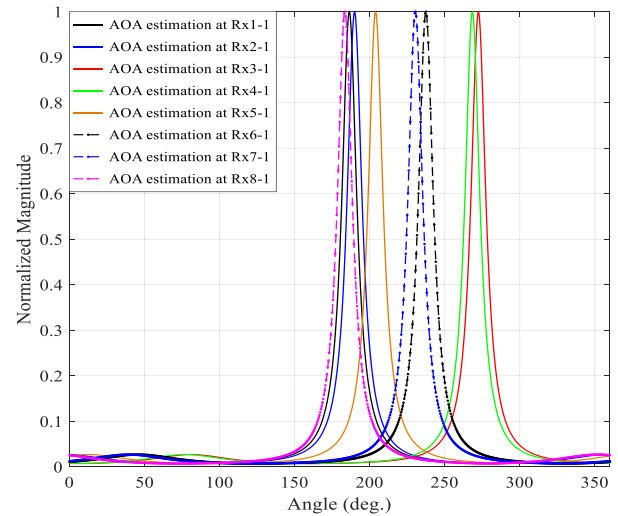
(b)

Fig. 13. Estimated AOA at each movement using the PV method. (a) Direction estimation using Tr_1. (b) Direction estimation using Tr_2.

TABLE VI

SHOWING THE RSS, $\hat{\phi}_m$, THE MEAN ACTUAL DIRECTION (ϕ_m), AND THE ABSOLUTE ESTIMATION ERROR AT EACH MOVEMENT

Move No.	RSS (dBm)	$\hat{\phi}_m$ (deg.)	ϕ_m (deg.)	err (deg.)
Rx1-1	-137.343	186.24º	183.95º	2.29º
Rx2-1	-133.041	203.62º	204.95º	1.33º
Rx3-1	-120.067	271.74º	270.28º	1.46º
Rx4-1	-110.203	269.12º	264.84º	4.28º
Rx5-1	-92.390	206.18º	199.72º	7.46º
Rx6-1	-74.248	249º	240.15º	8.85º
Rx7-1	-67.517	233.56º	231.44º	2.12º
Rx8-1	-53.049	185.12º	185.71º	0.59º

the vehicle was traveling in the correct direction toward the object.

The performance of the PV method using both Tr_1 and Tr_2 through these positions is depicted in Fig. 13. As illustrated, this method provides sharp peaks and accurate estimation using only three sensors. The overall performance of the
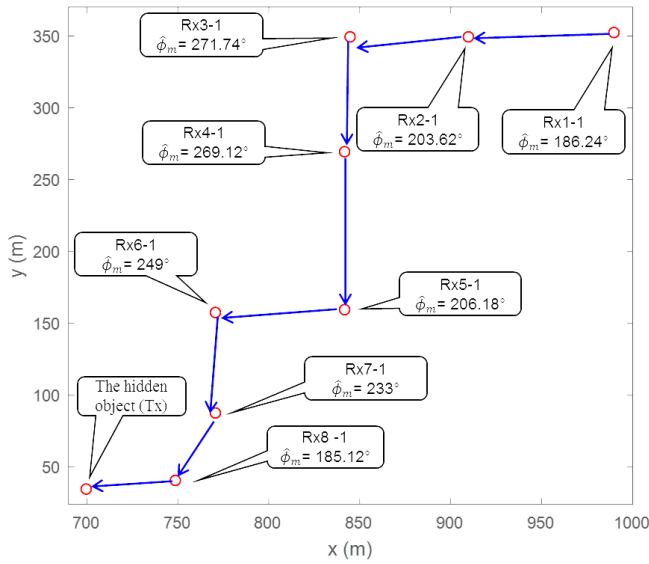
Fig. 14. Overall tracking system performance.

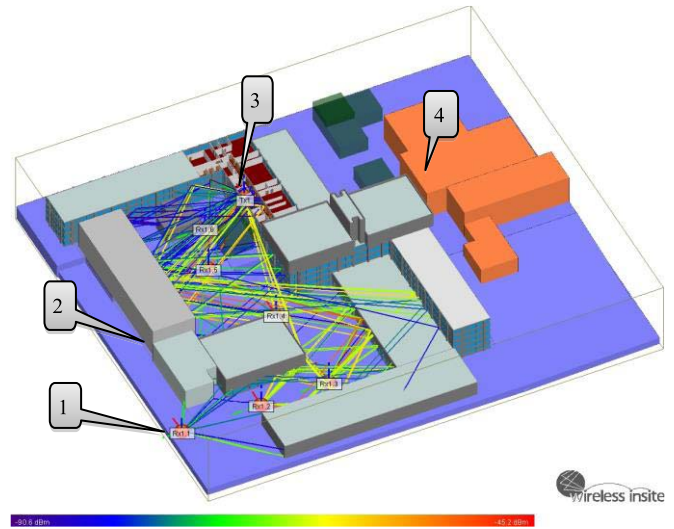Fig. 15. University of Bradford campus (eastern half).

Fig. 16. Showing outdoor–indoor tracking scenario; 1 is the starting point of the tracking process, 2 is the Horton Building, 3 is the location of the hidden object at the fifth floor inside the Chesham B Block, and 4 is the fitness and lifestyle building.

system can be presented based on the locations of the receiver at all the measurement points, indicated by red circles, and the corresponding mean estimated directions at these points, as shown in Fig. 14. The blue arrows represent the route of the vehicle movement during the tracking process. This system is suitable to be placed above a mobile vehicle to work as a base station for tracking and search applications. Therefore, it is a powerful tool to adopt for such applications.

D. Outdoor-to-Indoor Localization Scenario

This scenario investigates the performance of the localization system to deduce, for emergency or security applications, the position of an agent located inside a building. Since the tracking process, typically starts from outside and most of the buildings consist of many floors, the estimation of both azimuth and elevation angles was required to ensure accurate localization. In this scenario, the eastern half of the campus of the University of Bradford (U.K.), illustrated in Fig. 15, was considered. The campus was modeled using the Wireless-InSite software, as shown in Fig. 16. All the relevant building materials, for instance, brick, concrete, glass, wood, and other materials were taken into account in the testbed model. Further to this, the permittivity and conductivity of these

materials were calculated and inserted in the Wireless InSite software to ensure an accurate simulation process.

It is noteworthy that, as the number of paths increased, and the differences in power between these paths decreased, the decisions about direction became more difficult. The higher frequency (f = 837 MHz) band was chosen and therefore all six elements of the spiral sensor array could be exploited in the signal processing stage. An omnidirectional transmitter antenna was placed at point 3, as shown in Fig. 16, whereas the receiver was assumed located 1.5 m above the ground, as illustrated at point 1 in Fig. 16.

As this type of environment suffers from intensive multiple propagation paths, the tracking process in this scenario uses the same criteria to support the direction of the movement such as the earliest TOA path, the strongest path, and so on. The mean estimated angles $(\hat{\theta}_m, \hat{\phi}_m) = \left((\sum_{i=1}^{4} \hat{\theta}_i/4), (\sum_{i}^{4} \hat{\phi}_i/4) \right)$ were used as the ultimate decision to move from one place to another. The tracking process started by receiving the channel response and this was then processed using the OFDM modulation scheme over 5 MHz bandwidth: this was divided into 32 subcarriers. After this, the IFFT technique was applied to the received channel transfer function to acquire the impulse response with ten paths. Next, the received data matrix was constructed and a decoupling method applied. Finally, the PV method was used to determine the direction of the received signal paths. The RSS was also measured in this scenario for the same reason as in the previous scenario.

The first measurement in the tracking process was at point Rx1.1 (i.e., No. 1 in Fig. 16). The estimated AOA based on the least TOA subcarrier criteria indicated a line in the direction of the hidden transmitter appearing to be inside the Horton block, No. 2 in Fig. 16. However, the estimated angles at this point, taking account of all the other criteria, showed the received paths coming from different directions, as given in Table VII and Fig. 17(a). Hence, the movement decision based on the mean estimated angles was to move forward and another measurement was then taken at point Rx1.2. At this point, the measured directions were used to determine the next movement forward in the direction of

TABLE VII
ESTIMATED ANGLES AT EACH MOVE BASED ON SEVERAL SCENARIOS

Move No.	$(\hat{\theta}_1, \hat{\phi}_1)$	$(\hat{\theta}_2, \hat{\phi}_2)$	$(\hat{\theta}_3, \hat{\phi}_3)$	$(\hat{\theta}_4, \hat{\phi}_4)$
Rx1.1	(90°, 150°)	(63°, 96°)	(80°, 92°)	(53°, 107°)
Rx1.2	(90°, 54°)	(90°, 127°)	(76°, 95°)	(71°, 99.5°)
Rx1.3	(78°, 157.5°)	(90°, 150.5°)	(69°, 247°)	(63°, 241.5°)
Rx1.4	(78°, 155.5°)	(79°, 154°)	(90°, 295°)	(90°, 191.5°)
Rx1.5	(71.5°, 89°)	(74°, 109.5°)	(73°, 119.5°)	(72.5°, 101°)
Rx1.6	(64.5°, 104°)	(50°, 82.5°)	(59°, 130°)	(90°, 80°)

TABLE VIII
SHOWING THE RSS AND MEAN ESTIMATED ANGLES $(\hat{\theta}_m, \hat{\phi}_m)$

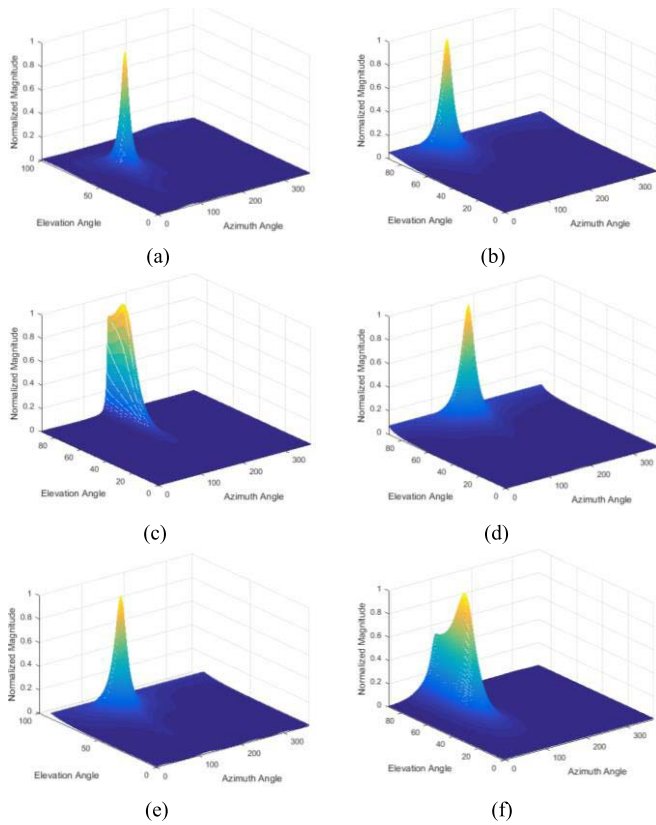| Move No.	RSS (dBm)	$(\hat{\theta}_m, \hat{\phi}_m)$
a. Rx1.1	-72.525	(71.5°, 111.25°)
b. Rx1.2	-67.604	(81.75°, 93.87°)
c. Rx1.3	-58.037	(75°, 199.12°)
d. Rx1.4	-53.398	(84.25°, 199°)
e. Rx1.5	-49.486	(72.75°, 104.5°)
f. Rx1.6	-46.053	(65.87°, 99.25°)

Fig. 17. 3-D estimated AOAs with the outdoor–indoor scenario. (a) First move at Rx1.1 point. (b) Second move at Rx1.2 point. (c) Third move at Rx1.3 point. (d) Fourth move at Rx1.4 point. (e) Fifth move at Rx1.5 point. (f) Sixth move at Rx1.6 point.

the transmitter. The estimation performance of the scheme is depicted in Fig. 17(b): the movement decision was also to move forward and the third measurement was considered at point Rx1.3. The performance estimation at this point is depicted in Fig. 17(c), while the estimated angles based on each criterion are presented in Table VII. Based on the mean estimated angles in Table VIII, the direction of the movement has been changed by 90°. The measured RSS at this point, −58 dBm, when compared to the previous readings (−72.5 and −67.6 dBm, respectively), verified that the receiver is approaching the location of the hidden object.

At Rx1.4, the computed angles based on the least TOA subcarrier, the strongest subcarrier, and averaging all of the subcarriers indicated that the tracked object existed inside the Chesham B block (No. 3 in Fig. 16) as shown in Fig. 17(d) and Table VII. However, the computed angles, based on the averaging of the five strongest subcarriers, indicated the hidden

object to be inside the Horton building. As it was clear that the test environment suffered from extensive multipath propagation effects, another new measurement was required to ensure accurate localization. Hence, based on the obtained values of $\hat{\theta}_m$ and $\hat{\phi}_m$ at this point, the movement direction was altered by 20°. The next reading was taken at point Rx1.5.

The obtained direction at this point confirmed that the hidden object was indeed located inside the Chesham building, as given in Fig. 17(e). To make sure that the estimation was correct, another movement was added, namely, at the Rx1.6 point. The direction now obtained confirmed the hidden object to be inside the Chesham building. This can be seen clearly from Fig. 17(f) and the recorded results in Tables VII and VIII. Based on the above argument and according to the results given in Fig. 17 and Table VIII, the scheme has determined the location of the hidden object, overcoming multipath effects. The proposed scheme roughly determined the position of the tracked object at the fourth move [see Fig. 17(d)] and then finally confirmed that at points Rx1.5 and Rx1.6 [see Fig. 17(e) and (f)].

VII. CONCLUSION

In this article, a dual-band compact-size and low complexity localization system has been proposed for outdoor and outdoor–indoor tracking applications, based on an efficient AOA method and using small omnidirectional spiral antennas suitable for possible integration on top of vehicles. A sensor array geometry, which is capable of working in dual-band mode simultaneously, was modeled, and a superposition theory for two different triangular subarrays was applied to enhance the performance of the proposed tracking system at the lower frequency. An OFDM modulation scheme over a wideband spectrum was used to improve the performance of the tracking system. Decoupling was applied to compensate for MC and hence to improve the estimation accuracy. The proposed system, based on the PV algorithm, was used to track a moveable object in a realistic simulation and compared with many popular existing AOA techniques. The obtained results verified the effectiveness and strength of the PV technique for such applications. Two localization scenarios were implemented: outdoor to outdoor and outdoor to indoor, using single measurements under multipath propagation conditions to evaluate and test the proposed tracking system performance. Decisions on the movement of the tracker from one position to another considered the earliest TOA subcarrier, the highest subcarrier power, and the average of some and all of the arrival subcarriers to support the estimated direction for the tracking process. The RSS was read and used as an extra tool to make sure the receiver movement was on the correct route. The results demonstrated that the proposed scheme worked efficiently, with far lower processing requirements (and hence greater speed) than alternative strategies.

APPENDIX A

DEVIATION OF (47)

The parameters of (47) have been derived and the results can be given as follows:

$$G = \begin{bmatrix} G_1 & G_2 \\ G_2^T & G_3 \end{bmatrix} \quad (A.1)$$

G_1, G_2, and G_3 can be obtained as follows:

$$G_1 = c_1 \sum_{i=1}^{M} \bar{A}_i^T \bar{A}_i + c_2 \sum_{i=1}^{M} \tilde{A}_i^T \tilde{A}_i \quad (A.2)$$

$$G_2 = -c_1 \sum_{i=1}^{M} \bar{A}_i^T \tilde{A}_i + c_2 \sum_{i=1}^{M} \tilde{A}_i^T \bar{A}_i \quad (A.3)$$

$$G_3 = c_1 \sum_{i=1}^{M} \tilde{A}_i^T \tilde{A}_i + c_2 \sum_{i=1}^{M} \bar{A}_i^T \bar{A}_i \quad (A.4)$$

c_1 and c_2 can be calculated using the formulas below

$$c_1 = \int_{+\infty}^{-\infty} \int_{-\infty}^{+\infty} \frac{y_1^2}{f(e)} d\bar{e}d\tilde{e} \quad (A.5)$$

$$c_2 = \int_{+\infty}^{-\infty} \int_{-\infty}^{+\infty} \frac{y_2^2}{f(e)} d\bar{e}d\tilde{e} \quad (A.6)$$

y_1 and y_2 can be defined as follows:

$$y_1 = \mathcal{M} \sum_{j=1}^{T} e^{-\bar{u}} \bar{u} \sum_{j=1}^{T} e^{-\tilde{u}} \quad (A.7)$$

$$y_2 = \mathcal{M} \sum_{j=1}^{T} e^{-\bar{u}} \sum_{j=1}^{T} e^{-\tilde{u}} \tilde{u} \quad (A.8)$$

$$\Delta_t = \begin{bmatrix} \Delta_{t1} \\ \Delta_{t2} \end{bmatrix} \quad (A.9)$$

Δ_{t1} and Δ_{t2} can be computed as given below:

$$\Delta_{t1} = c_1 \sum_{i=1}^{M} \left(\bar{A}_i^T \bar{\mathcal{Q}}(t) \bar{D}_i - \bar{A}_i^T \tilde{\mathcal{Q}}(t) \tilde{D}_i \right)$$
$$+ c_2 \sum_{i=1}^{M} \left(\tilde{A}_i^T \tilde{\mathcal{Q}}(t) \bar{D}_i + \tilde{A}_i^T \bar{\mathcal{Q}}(t) \tilde{D}_i \right) \quad (A.10)$$

$$\Delta_{t2} = -c_1 \sum_{i=1}^{M} \left(\tilde{A}_i^T \bar{\mathcal{Q}}(t) \bar{D}_i - \tilde{A}_i^T \tilde{\mathcal{Q}}(t) \tilde{D}_i \right)$$
$$+ c_2 \sum_{i=1}^{M} \left(\bar{A}_i^T \tilde{\mathcal{Q}}(t) \bar{D}_i + \bar{A}_i^T \bar{\mathcal{Q}}(t) \tilde{D}_i \right) \quad (A.11)$$

where

$$\mathcal{Q}(t) = \mathscr{G}(t)^H \mathscr{G}(t)$$
$$D_i = [D_1^T \quad D_2^T \cdots \cdots D_M^T]$$
$$D_i = \left[\frac{\partial A_{i1}}{\partial \theta_1} \cdots \cdots \frac{\partial A_{iK}}{\partial \theta_K} \right], \quad i = 1, \ldots K.$$

Finally, Υ can be given as described below:

$$\Upsilon = \sum_{t=1}^{L} c_1 \begin{pmatrix} \bar{D}^T \bar{\mathcal{Q}}(t)^T \bar{\mathcal{Q}}(t) \bar{D} - \bar{D}^T \bar{\mathcal{Q}}(t)^T \tilde{\mathcal{Q}}(t) \tilde{D} \\ -\tilde{D}^T \tilde{\mathcal{Q}}(t)^T \bar{\mathcal{Q}}(t) \bar{D} + \tilde{D}^T \tilde{\mathcal{Q}}(t)^T \bar{\mathcal{Q}}(t) \tilde{D} \end{pmatrix}$$

$$+ \sum_{t=1}^{L} c_2 \begin{pmatrix} \bar{D}^T \bar{\mathcal{Q}}(t)^T \bar{\mathcal{Q}}(t) \bar{D} + \bar{D}^T \bar{\mathcal{Q}}(t)^T \tilde{\mathcal{Q}}(t) \tilde{D} \\ +\tilde{D}^T \tilde{\mathcal{Q}}(t)^T \bar{\mathcal{Q}}(t) \bar{D} + \tilde{D}^T \tilde{\mathcal{Q}}(t)^T \bar{\mathcal{Q}}(t) \tilde{D} \end{pmatrix}. \quad (A.12)$$

When $\bar{m}(t)$ and $\tilde{m}(t)$ have the same distribution, then

$$c_1 = c_2 = \int_{+\infty}^{-\infty} \int_{-\infty}^{+\infty} \frac{y_1^2}{f(e)} d\bar{e}d\tilde{e} \quad (A.13)$$

$$G = \begin{bmatrix} \bar{G} & -\tilde{G} \\ \tilde{G} & \bar{G} \end{bmatrix} \quad (A.14)$$

$$\Upsilon = c_1 \sum_{t=1}^{L} Re\{ D^H \mathcal{Q}(t)^H \mathcal{Q}(t) D \} \quad (A.15)$$

$$G = c_1 A^H A \quad (A.16)$$

$$\Delta(t) = c_1 A^H \mathcal{Q}(t) D. \quad (A.17)$$

Many numerical methods can be used to solve c_1; however, one can exploit the MATLAB function "dblquad" to obtain c_1. When nonGaussian noise goes to zero [i.e., $m(t)$], then, $m \rightarrow 0$, $\bar{\varrho} \rightarrow 0$, $\tilde{\varrho} \rightarrow 0$ and therefore, the limit of (41) becomes as follows:

$$\lim_{m(t) \rightarrow 0} f_{e_i}(e_i(t)) = \frac{1}{\pi \sigma^2} e^{\left(-\frac{\bar{n}_i(t)^2}{\sigma^2} \right)} e^{\left(-\frac{\tilde{n}_i(t)^2}{\sigma^2} \right)}. \quad (A.18)$$

The limit of (A.7) is

$$\lim_{m(t) \rightarrow 0} y_1 = \frac{1}{\pi \sigma^2} e^{\left(-\frac{\bar{n}_i(t)^2}{\sigma^2} \right)} \left(\frac{\bar{n}_i(t)^2}{\sigma^2/2} \right) e^{\left(-\frac{\tilde{n}_i(t)^2}{\sigma^2} \right)}. \quad (A.19)$$

By substituting (A.18) and (A.19) into (A.13) and taking the limit yields

$$\lim_{m(t) \rightarrow 0} c_1 = \lim_{m(t) \rightarrow 0} \int_{+\infty}^{-\infty} \int_{-\infty}^{+\infty} \frac{y_1^2}{f(e)} d\bar{e}d\tilde{e} = \frac{2}{\sigma^2}. \quad (A.20)$$

Under these conditions, (48) becomes as follows:

$$CRLB(\theta) = \frac{\sigma^2}{2L} \left(\sum_{t=1}^{L} Re\{ D^H W \mathcal{Q}(t) D \} \right)^{-1} \quad (A.21)$$

where $\mathcal{W} = I - A(A^H A)^{-1} A^H$.

REFERENCES

[1] S. Su *et al.*, "Investigation of the relationship between tracking accuracy and tracking distance of a novel magnetic tracking system," *IEEE Sensors J.*, vol. 17, no. 15, pp. 4928–4937, Aug. 2017.

[2] M. A. Khan, N. Saeed, A. W. Ahmad, and C. Lee, "Location awareness in 5G networks using RSS measurements for public safety applications," *IEEE Access*, vol. 5, pp. 21753–21762, 2017.

[3] S. Xu, K. Doğançay, and H. Hmam, "3D AOA target tracking using distributed sensors with multi-hop information sharing," *Signal Process.*, vol. 144, pp. 192–200, Mar. 2018.

[4] Y. Fang, C. Wang, W. Yao, X. Zhao, H. Zhao, and H. Zha, "On-road vehicle tracking using part-based particle filter," *IEEE Trans. Intell. Transp. Syst.*, vol. 20, no. 12, pp. 4538–4552, Dec. 2019.

[5] *Federal Communications Commission*. Accessed: Feb. 20, 2018. [Online]. Available: http://www.fcc.gov/e911/

[6] H. Kloeden, D. Schwarz, E. M. Biebl, and R. H. Rasshofer, "Vehicle localization using cooperative RF-based landmarks," in *Proc. IEEE Intell. Vehicles Symp. (IV)*, Jun. 2011, pp. 387–392.

[7] G. De Angelis, G. Baruffa, and S. Cacopardi, "GNSS/cellular hybrid positioning system for mobile users in urban scenarios," *IEEE Trans. Intell. Transp. Syst.*, vol. 14, no. 1, pp. 313–321, Mar. 2013.

[8] D. Jourdan, D. Dardari, and M. Win, "Position error bound for UWB localization in dense cluttered environments," *IEEE Trans. Aerosp. Electron. Syst.*, vol. 44, no. 2, pp. 613–628, Apr. 2008.

[9] P. W. Ward, J. W. Betz, C. J. Hegarty, and E. D. Kaplan, "Satellite signal acquisition, tracking, and data demodulation," in *Understanding GPS: Principles and Applications*, Norwood, MA, USA: Artech House, 2006, pp. 153–241.

[10] S. Gezici *et al.*, "Localization via ultra-wideband radios: A look at positioning aspects for future sensor networks," *IEEE Signal Process. Mag.*, vol. 22, no. 4, pp. 70–84, Jul. 2005.

[11] R. Karlsson and F. Gustafsson, "The future of automotive localization algorithms: Available, reliable, and scalable localization: Anywhere and anytime," *IEEE Signal Process. Mag.*, vol. 34, no. 2, pp. 60–69, Mar. 2017.

[12] R. Mautz, "The challenges of indoor environments and specification on some alternative positioning systems," in *Proc. 6th Workshop Positioning, Navigat. Commun.*, Mar. 2009, pp. 29–36.

[13] S. A. Ahson and M. Ilyas, *Location-Based Services Handbook: Applications, Technologies, and Security*. Boca Raton, FL, USA: CRC Press, 2011.

[14] D. Fagan and R. Meier, "Intelligent time of arrival estimation," in *Proc. IEEE Forum Integr. Sustain. Transp. Syst.*, Jun. 2011, pp. 60–66.

[15] S. Gezici, "A survey on wireless position estimation," *Wireless Pers. Commun.*, vol. 44, no. 3, pp. 263–282, Feb. 2008.

[16] C. Xu, J. He, X. Zhang, P.-H. Tseng, and S. Duan, "Toward near-ground localization: Modeling and applications for TOA ranging error," *IEEE Trans. Antennas Propag.*, vol. 65, no. 10, pp. 5658–5662, Oct. 2017.

[17] N. Alam and A. G. Dempster, "Cooperative positioning for vehicular networks: Facts and future," *IEEE Trans. Intell. Transp. Syst.*, vol. 14, no. 4, pp. 1708–1717, Dec. 2013.

[18] A. Bensky, *Wireless Positioning Technologies and Applications*. Boston, MA, USA: Artech House, 2008.

[19] H. C. So, Y. T. Chan, and F. K. W. Chan, "Closed-form formulae for time-difference-of-arrival estimation," *IEEE Trans. Signal Process.*, vol. 56, no. 6, pp. 2614–2620, Jun. 2008.

[20] A. H. Sayed, A. Tarighat, and N. Khajehnouri, "Network-based wireless location: Challenges faced in developing techniques for accurate wireless location information," *IEEE Signal Process. Mag.*, vol. 22, no. 4, pp. 24–40, Jul. 2005.

[21] S.-F. Chuang, W.-R. Wu, and Y.-T. Liu, "High-resolution AoA estimation for hybrid antenna arrays," *IEEE Trans. Antennas Propag.*, vol. 63, no. 7, pp. 2955–2968, Jul. 2015.

[22] Y. Shen and M. Z. Win, "Fundamental limits of wideband localization—Part I: A general framework," *IEEE Trans. Inf. Theory*, vol. 56, no. 10, pp. 4956–4980, Oct. 2010.

[23] S. W. Chen, C. K. Seow, and S. Y. Tan, "Virtual reference device-based NLOS localization in multipath environment," *IEEE Antennas Wireless Propag. Lett.*, vol. 13, pp. 1409–1412, 2014.

[24] D. Inserra and A. M. Tonello, "A frequency-domain LOS angle-of-arrival estimation approach in multipath channels," *IEEE Trans. Veh. Technol.*, vol. 62, no. 6, pp. 2812–2818, Jul. 2013.

[25] G. Wang, J. Xin, J. Wang, N. Zheng, and A. Sano, "Subspace-based two-dimensional direction estimation and tracking of multiple targets," *IEEE Trans. Aerosp. Electron. Syst.*, vol. 51, no. 2, pp. 1386–1402, Apr. 2015.

[26] Y. Shen and M. Win, "On the accuracy of localization systems using wideband antenna arrays," *IEEE Trans. Commun.*, vol. 58, no. 1, pp. 270–280, Jan. 2010.

[27] M. Li and K.-M. Luk, "A low-profile wideband planar antenna," *IEEE Trans. Antennas Propag.*, vol. 61, no. 9, pp. 4411–4418, Sep. 2013.

[28] S. Zhu, D. G. Holtby, K. L. Ford, A. Tennant, and R. J. Langley, "Compact low frequency varactor loaded tunable SRR antenna," *IEEE Trans. Antennas Propag.*, vol. 61, pp. 2301–2304, 2013.

[29] M. A. G. Al-Sadoon *et al.*, "The effects of mutual coupling within antenna arrays on angle of arrival methods," in *Proc. Loughborough Antennas Propag. Conf. (LAPC)*, Nov. 2016, pp. 1–5.

[30] W. Hong and K. Sarabandi, "Low profile miniaturized planar antenna with omnidirectional vertically polarized radiation," *IEEE Trans. Antennas Propag.*, vol. 56, no. 6, pp. 1533–1540, Jun. 2008.

[31] Remcom. *Wireless InSite 3D Wireless Prediction Software*. [Online]. Available: https://www.remcom.com/wireless-insite-em-propagation-software/

[32] L. Zuo, J. Pan, and Z. Shen, "Analytical algorithm for 3-D localization of a single source with uniform circular array," *IEEE Antennas Wireless Propag. Lett.*, vol. 17, no. 2, pp. 323–326, Feb. 2018.

[33] W. Hong and K. Sarabandi, "Low-profile, multi-element, miniaturized monopole antenna," *IEEE Trans. Antennas Propag.*, vol. 57, no. 1, pp. 72–80, Jan. 2009.

[34] H. T. Hui, "A new definition of mutual impedance for application in dipole receiving antenna arrays," *IEEE Antennas Wireless Propag. Lett.*, vol. 3, pp. 364–367, 2004.

[35] T. S. Ghazaany *et al.*, "Coupling compensation of the antenna array response for direction finding applications," in *Proc. 9th IET Int. Conf. Comput. Electromagn. (CEM)*, 2014, pp. 1–2.

[36] Y.-H. Cao, X.-G. Xia, and S.-H. Wang, "IRCI free colocated MIMO radar based on sufficient cyclic prefix OFDM waveforms," *IEEE Trans. Aerosp. Electron. Syst.*, vol. 51, no. 3, pp. 2107–2120, Jul. 2015.

[37] D. Karampatsis, "Modelling and performances assessment of OFDM and fast-OFDM wireless communication systems," Ph.D. dissertation, Univ. London, London, U.K., 2004.

[38] Y. S. Cho, J. Kim, W. Y. Yang, and C. G. Kang, *MIMO-OFDM Wireless Communications With MATLAB*. Hoboken, NJ, USA: Wiley, 2010.

[39] R. Shafin, L. Liu, J. Zhang, and Y.-C. Wu, "DoA estimation and capacity analysis for 3-D millimeter wave Massive-MIMO/FD-MIMO OFDM systems," *IEEE Trans. Wireless Commun.*, vol. 15, no. 10, pp. 6963–6978, Oct. 2016.

[40] Z.-M. Liu, "Conditional Cramér–Rao lower bounds for DOA estimation and array calibration," *IEEE Signal Process. Lett.*, vol. 21, no. 3, pp. 361–364, Mar. 2014.

[41] M. Pesavento and A. B. Gershman, "Maximum-likelihood direction-of-arrival estimation in the presence of unknown nonuniform noise," *IEEE Trans. Signal Process.*, vol. 49, no. 7, pp. 1310–1324, Jul. 2001.

[42] A. Gershman, P. Stoica, M. Pesavento, and E. G. Larsson, "Stochastic Cramér–Rao bound for direction estimation in unknown noise fields," *IEE Proc. Radar, Sonar Navigat.*, vol. 149, pp. 2–8, Feb. 2002.

[43] P. Stoica and A. Nehorai, "MUSIC, maximum likelihood, and Cramér–Rao bound," *IEEE Trans. Acoust., Speech, Signal Process.*, vol. 37, no. 5, pp. 720–741, May 1989.

[44] S. A. Vorobyov, A. B. Gershman, and K. M. Wong, "Maximum likelihood direction-of-arrival estimation in unknown noise fields using sparse sensor arrays," *IEEE Trans. Signal Process.*, vol. 53, no. 1, pp. 34–43, Jan. 2005.

[45] A. Elgammal, R. Duraiswami, D. Harwood, and L. S. Davis, "Background and foreground modeling using nonparametric kernel density estimation for visual surveillance," *Proc. IEEE*, vol. 90, no. 7, pp. 1151–1163, Jul. 2002.

[46] Y. Zhang, Q. Wan, H.-P. Zhao, and W.-L. Yang, "Support vector regression for basis selection in Laplacian noise environment," *IEEE Signal Process. Lett.*, vol. 14, no. 11, pp. 871–874, Nov. 2007.

[47] S. M. Kay, *Fundamentals of Statistical Signal Processing*. Upper Saddle River, NJ, USA: Prentice-Hall, 1993.

[48] H. Abeida and J. P. Delmas, "Direct derivation of the stochastic CRB of DOA estimation for rectilinear sources," *IEEE Signal Process. Lett.*, vol. 24, no. 10, pp. 1522–1526, Oct. 2017.

[49] B. M. Sadler and R. J. Kozick, "Maximum-likelihood array processing in non-Gaussian noise with Gaussian mixtures," *IEEE Trans. Signal Process.*, vol. 48, no. 12, pp. 3520–3535, 2000.

[50] J. Capon, "High-resolution frequency-wavenumber spectrum analysis," *Proc. IEEE*, vol. 57, pp. 1408–1418, Aug. 1969.

[51] R. Kumaresan and D. W. Tufts, "Estimating the angles of arrival of multiple plane waves," *IEEE Trans. Aerosp. Electron. Syst.*, vol. AES-19, no. 1, pp. 134–139, Jan. 1983.

[52] R. Schmidt, "Multiple emitter location and signal parameter estimation," *IEEE Trans. Antennas Propag.*, vol. AP-34, no. 3, pp. 276–280, Mar. 1986.

[53] S. Marcos, A. Marsal, and M. Benidir, "The propagator method for source bearing estimation," *Signal Process.*, vol. 42, no. 2, pp. 121–138, Mar. 1995.

[54] R. Grover, D. A. Pados, and M. J. Medley, "Subspace direction finding with an auxiliary-vector basis," *IEEE Trans. Signal Process.*, vol. 55, no. 2, pp. 758–763, Jan. 2007.

[55] H. Semira, H. Belkacemi, and S. Marcos, "High-resolution source localization algorithm based on the conjugate gradient," *EURASIP J. Adv. Signal Process.*, vol. 2007, no. 1, p. 12, Dec. 2007.

[56] Z. Yang, L. Xie, and C. Zhang, "Off-grid direction of arrival estimation using sparse Bayesian inference," *IEEE Trans. Signal Process.*, vol. 61, no. 1, pp. 38–43, Jan. 2013.

[57] J. Dai, X. Bao, W. Xu, and C. Chang, "Root sparse Bayesian learning for off-grid DOA estimation," *IEEE Signal Process. Lett.*, vol. 24, no. 1, pp. 46–50, Jan. 2017.

Mohammed Abdullah Ghali Al-Sadoon (Member, IEEE) received the B.Sc. and M.Sc. degrees from the University of Basrah, Basrah, Iraq, in 2008 and 2011, respectively, and the Ph.D. degree from the University of Bradford, Bradford, U.K., in 2020. In 2015, he obtained a scholarship from the Higher Committee for Education Development (HCED), Iraq, to complete his Ph.D. degree.

In 2011, he worked as an Electrical and Control Engineer at Ministry of Oil, South Oil Company (SOC), Basrah. From 2013 to 2015, he was appointed as a Lecturer with the Department of Communication and Informatics Engineering, Basrah University College of Science and Technology, Basrah. During his Ph.D. research, he worked on many projects that focused on combining new and modern RF direction-finding methods for covert tracking and localization applications using advanced signal processing techniques. He is the author of five chapters and has published over 30 academic journal and conference papers. His main research interests are now concentrated on the multiple-antenna technologies, signal processing, and localization, including RF and antenna design for direction-finding applications and medical implanted wireless communications.

Dr. Al-Sadoon is a member of the Institution of Engineering and Technology (IET). He received the Best Innovative Engineering Conference Paper 2017 and 2018 in the 1st and 2nd Annual Innovative Engineering Research Conference, University of Bradford, and the Best Paper presented at the 7th International Conference on Internet Technologies and Application (ITA2017). He is an Associate Fellow of the Higher Education Academy, U.K. He is also a reviewer for several high impacts and respected journals and magazines, including the IEEE TRANSACTION journals, IET journals, and Multidisciplinary Digital Publishing Institute (MDPI) journals.

Rameez Asif was born in Lahore, Pakistan. He received the B.Eng. degree in electronics and computer engineering from the University of Delaware, Newark, DE, USA, in 2010, and the M.Sc. degree (Hons.) in electrical and electronics engineering and the Ph.D. degree in RF and microwave engineering from the University of Bradford, Bradford, U.K., in 2012 and 2018, respectively.

In his last job, he was the Senior RF Design Engineer at Visibility Asset Management Limited, Arris, U.K. He is currently a Post-Doctoral Research Assistant with the Future Ubiquitous Networks (FUN) Research Group, Arris, U.K. He has been a Microsoft Certified System Engineer (MCSE) since 2000. He owns a patent for the radiation shield since 2018. The shield is used to diminish penetrations of the electromagnetic waves in the human brain from the Global System for Mobile Communications (GSM) mobile handsets. He has published several journals and conference papers. His main research interests are digital signal processing, ray tracing, wireless sensor networks, image processing, meta-materials, and their applications, Multi-User Multiple Input Multiple Output (MU-MIMO), wireless sensor networks, electrically small antennas, and radio frequency identification (RFID).

Dr. Asif became a Student Member of the Institution of Engineering and Technology (IET) in 2011. He is an Associate Fellow of the Higher Education Academy. He is also the Technical Editor of the Multidisciplinary Digital Publishing Institute (MDPI), future Internet journal, and also serves as a reviewer for the several IEEE TRANSACTION journals.

Yasir Ismael Abdulraheem Al-Yasir (Member, IEEE) received the B.Sc. and M.Sc. degrees in electrical engineering from the University of Basrah, Basrah, Iraq, in 2012 and 2015, respectively. He is currently pursuing the Ph.D. degree with the Radio Frequency and Sensor Design Research Group, University of Bradford, Bradford, U.K.

In 2014, he joined the research team of the Antennas and RF Engineering Research Group, University of Bradford, as a Research Visitor for four months. In 2015, he was appointed as a Lecturer with the Iraq University College, Southern Technical University, Basrah. In 2016 and 2017, he was working as an Electrical Engineer at Basra Oil Training Institute, Ministry of Oil, Basrah. Since January 2018, he has been an Early Stage Researcher with the University of Bradford, where he is also working with eight research groups, spread across four leading universities/research institutions and four industrial partners in five different European countries, targeting the 5G mobile handset and funded by the European Union's Horizon 2020 research and innovation program. He has authored one book and five chapters and published more than 80 journal and conference papers on aspects of wireless communications. His main interests are filters, antennas, and RF and microwave circuits.

Mr.Mr. Al-Yasir was a recipient of the Best Paper Award at the IEEE 2nd 5G World Forum and the IEEE 4th 5G Summit, Dresden, Germany.

Raed A. Abd-Alhameed (Senior Member, IEEE) is currently a Professor of electromagnetic and radio frequency engineering with the University of Bradford, Bradford, U.K. He is also the Leader of radio frequency, propagation, sensor design, and signal processing. In addition, he is also leading the Communications Research Group for years within the School of Engineering and Informatics, University of Bradford. He is also a Chartered Engineer. He has long years' research experience in the areas of radio frequency, signal processing, propagations, antennas, and electromagnetic computational techniques. He has published over 600 academic journals and conference papers. In addition, he has coauthored five books and several book chapters. He is also a principal investigator for several funded applications to Engineering and Physical Sciences Research Council (EPSRC) and the leader of several successful knowledge transfer programs, such as Arris (previously known as Pace Plc), Yorkshire Water Plc, U.K., Harvard Engineering Plc, USA, IETG Ltd., USA, Seven Technologies Group, U.K., Emkay Ltd., U.K., and Two World Ltd., U.K. He has also been a co-investigator in several funded research projects, including the H2020 Marie Skłodowska-Curie Actions: Research and innovation staff exchange (RISE): secure and wireless multimodal biometric scanning device for passenger verification targeting land and sea border control, the H2020 Marie Skłodowska-Curie Actions: Innovative training networks secure network coding for next generation mobile small cells 5G-US, the Nonlinear and demodulation mechanisms in biological tissue (Department of Health, Mobile Telecommunications and Health Research Programme), and the Assessment of the potential direct effects of cellular phones on the nervous system (EU: collaboration with six other major research organizations across Europe). He has also been a Research Visitor with Wrexham Glyndwr University, Wrexham, U.K., since 2009, covering the wireless and communications research areas. His research interests are in computational methods and optimizations, wireless and mobile communications, sensor design, electromagnetic compatibility (EMC), beam steering antennas, energy-efficient power amplifiers (PAs), and RF predistorter design applications.

Prof. Abd-Alhameed is a fellow of the Institution of Engineering and Technology and the Higher Education Academy. He was a recipient of the Business Innovation Award for his successful Knowledge Transfer Programme (KTP) with Pace and Datong companies on the design and implementation of MIMO sensor systems and antenna array design for service localizations. He is also the chair of several successful workshops on energy-efficient and reconfigurable transceivers: Approach toward energy conservation and CO_2 reduction that addresses the biggest challenges for the future wireless systems. He has been a co-editor of *Electronics MDPI Journal* since June 2019. In addition, he has been a Guest Editor of the *Institution of Engineering and Technology (IET) Science, Measurements and Technology Journal* since 2009.

Peter S. Excell (Life Senior Member, IEEE) received the B.Sc. degree in engineering science from the University of Reading, Reading, U.K., in 1970, the Ph.D. degree from the University of Bradford, Bradford, U.K., in 1980, and the D.Sc. degree from Wrexham Glyndwr University, Wrexham, U.K., and the University of Chester, Chester, U.K., in 2020.

Until 2007, he was an Associate Dean of research with the School of Informatics, University of Bradford, Bradford, U.K., where he is currently a Visiting Professor. He is also a Professor with the Emeritus of Communications, Wrexham Glyndwr University, where he was the Deputy Vice Chancellor until 2015. He is also a Chartered Engineer and a Chartered IT Professional. He has published over 500 articles. His academic interests are concentrated in the areas of wireless technologies, electromagnetics and antennas, plus broader interests in future communications applications, and technological evolution.

Dr. Excell is a fellow of the Institution of Engineering and Technology, the British Computer Society, and the Higher Education Academy; and a member of the Association for Computing Machinery, the Bioelectromagnetics Society, and the Applied Computational Electromagnetics Society.